

Department of Physics and Astronomy

University of Heidelberg

Master thesis

in Physics

submitted by

Aaron Spring

born in Frankfurt/Main

2017

Decadal variations in the Southern Ocean carbon sink in MPI-ESM 100 ensemble simulations

This Master thesis has been carried out by Aaron Spring
at the institute of Environmental Physics
under the supervision of
Prof. Dr. Norbert Frank
and
Dr. Tatiana Ilyina
from
Max Planck Institute for Meteorology, Hamburg,
Marine Biogeochemistry

ABSTRACT

Recent observations suggest pronounced decadal variations in the Southern Ocean carbon sink. However, due to the sparse spatial and temporal coverage, it is challenging to discern the dynamics of internally varying processes. Earth system models (ESMs), while being a useful tool to analyze processes that contribute to variability, rarely capture this variability. By analyzing a large ensemble of 100 historical simulations based on Max Planck Institute's ESM (MPI-ESM) starting from different initial conditions but using identical forcing, I assess modeled decadal internal variability.

The modeled decadal internal variability of the Southern Ocean carbon sink south of 35°S is quantified to 0.22 PgC/yr , compared to the absolute carbon sink of 1.15 PgC/yr and dominates over the forced trend of 0.02 PgC/yr . MPI-ESM Large Ensemble captures decadal variations of similar magnitude as suggested by observations. At the area of largest variability at $50\text{-}60^{\circ}\text{S}$, the CO_2 flux follows two wind-driven regimes: Stronger winds increase the upper-ocean overturning circulation, which enhances upwelling and hence outgassing of deep, carbon-rich waters, which weakens the carbon sink. For decreasing winds, the upper-ocean circulation slows down and hence strengthens the carbon sink.

ZUSAMMENFASSUNG

[Am Ende neu] Neue Beobachtungsdaten zeigen dekadische Schwankungen in der Kohlenstoffsenke im Südlichen Ozean auf. Auf Grund der spärlichen räumlichen und temporären Beobachtungsdatendichte, ist das Unterscheiden der Dynamik der variablen Prozesse herausfordernd. Erdsystemmodelle, die ein nützliches Hilfsmittel zum Analysieren von variablen Prozessen sind, erfassen selten diese internen Schwankungen. Durch das Analysieren eines Ensemble mit 100 historischen Simulationen basierend auf dem Max-Planck-Institut ESM (MPI-ESM) mit leicht veränderten Anfangsbedingungen untersuche ich modellierte interne Variabilität.

Die modellierte dekadische interne Variabilität der Kohlenstoffsenke im Südlichen Ozean südlich von 35°S beträgt $\sim 0.18 \text{ PgC/yr}$. Die 100 MPI-ESM Simulationen erfassen dekadische Trend von ähnlicher Stärke wie es die Beobachtungsdaten anregen. In der Region mit der höchsten Variabilität bei $50\text{-}60^{\circ}\text{S}$ ergeben sich zwei wind-getriebene Regime: Stärkere Winde steigern die obere Umweltzirkulation, was das Aufsteigen von kohlenstoffreichem Tiefenwasser verstärkt. Das

darauf folgene Ausgasen schwächt die Kohlenstoffsenke. Schwächerer Wind verlangsamen die Umwelzzirkulation und stärken somit die Kohlenstoffsenke.

CONTENTS

1	INTRODUCTION	1
2	METHODS	3
2.1	Model description of MPI-ESM	3
2.2	Large ensemble simulations	6
2.3	Observational data	8
2.4	Statistical methods	9
2.5	Climatological methods	10
3	MODEL EVALUATION IN THE SOUTHERN OCEAN	13
3.1	CO ₂ flux	13
3.2	Winds	17
3.3	Biology	20
3.4	Upper-Ocean Overturning Circulation	24
4	PROCESSES CORRESPONDING TO MULTI-YEAR TRENDS IN SEA-AIR CO ₂ FLUX	27
4.1	The role of westerly winds in Southern Ocean CO ₂ flux variability	27
4.2	Positive CO ₂ flux trends	30
4.3	Negative CO ₂ flux trends	37
5	CONTRIBUTION OF DIFFERENT PROCESSES TO MULTI-YEAR PCO ₂ TRENDS	43
5.1	Derivation of the framework	43
5.2	Estimate of pCO ₂ drivers	47
6	CONCLUSIONS AND OUTLOOK	55
A	APPENDIX	59

INTRODUCTION

The oceans are major carbon sink by taking up about 25-30% of the anthropogenic carbon emissions from the atmosphere [Sabine et al., 2004; Le Quéré et al., 2016]. As a key region, the Southern Ocean is estimated to contribute about 50% to the global ocean carbon sink [Takahashi et al., 2012].

Recent observations suggest pronounced decadal variations in the Southern Ocean carbon sink [Rödenbeck et al., 2013; Landschützer et al., 2015]. Understanding internal variability is important to understand whether the climate is changing due to different forcing or whether it just fluctuates [Hawkins and Sutton, 2009]. However, due to the sparse spatial and temporal coverage of measurement data, it is challenging to discern the dynamics of internally varying processes, which demands for the evaluation with models. Models, numerical representations of the climate system based on physical, biological and chemical principles, are a useful tool to analyze processes that contribute to variability.

By forcing an ocean model with atmospheric reanalysis data, Loven-duski et al., 2007, 2008 demonstrates that increased upwelling due to stronger and southward shifted westerly winds in the Southern hemisphere cause a decline in the Southern Ocean carbon sink.

Yet, Earth System Models ([ESMs](#)), containing a freely evolving coupled atmospheric and ocean component, don't capture the multi-year variations in sea-air CO₂ flux as suggest by observations [Wang et al., 2016]. Using a large ensemble of simulations with perturbed initial conditions but identical forcing and model allows to separate trends into an ensemble mean trend, the forced signal, and the residual, the internal variability [McKinley et al., 2016, 2017].

By using a large ensemble of 100 simulations based on the Max Planck Institute-Earth System Model (hereafter [MPI-ESM LE](#)), I investigate the decadal internal variability of oceanic carbon uptake to answer the following research questions:

- What is the modeled internal variability of the Southern Ocean carbon sink?
- What are the sources of internal variability?
- What are the contributions of different processes to multi-year trends in sea-air CO₂ flux?

Working on my research questions builds the outline for this thesis, which revisits the dominant processes leading to extreme trends in the Southern Ocean carbon sink in the biogeochemical model **HAMOCC** [similar Lovenduski et al., 2007, 2008]. This revisit is particularly interesting as other large ensembles of perturbed initial conditions do not capture strong decadal variations in the Southern Ocean carbon sink; whereas **MPI-ESM LE** does [private communication N. Lovenduski (**NCAR**) and S. Schlunegger (**GFDL**), see section 2.2 for details].

I use a large ensemble of **MPI-ESM** simulations (ch. 2) and evaluate the model in the key features related to the Southern Ocean carbon sink variability (ch. 3). Ch. 4 focuses the response of individual processes related to changes in Southern hemisphere winds, which are already discussed in the literature, e.g. pCO₂ temperature effect [Takahashi et al., 1993; Lovenduski et al., 2007], circulation [Abernathay et al., 2011; Hauck et al., 2013; Lauderdale et al., 2013; Lovenduski et al., 2008] and biology [Lovenduski and Gruber, 2005; Hauck et al., 2013; Tagliabue et al., 2014]. Ch. 5 quantitative assesses these responses on oceanic pCO₂. Finally, I draw my main conclusions and evaluate how relatable perturbed initial conditions large ensembles are for internal variability in observations and give an outlook on possible future research (ch. 6).

2

METHODS

2.1 MODEL DESCRIPTION OF MPI-ESM

The Max Planck Institute-Earth System Model (**MPI-ESM**) consists of coupled general circulation models of the atmosphere **ECHAM6** [Stevens et al., 2013] and ocean **MPIOM** [Jungclaus et al., 2013], as well as subsystem models for vegetation on land **JSBACH** [Reick et al., 2013] and for marine biogeochemistry **HAMOCC** [Ilyina et al., 2013]. The large ensemble simulations are based on **MPI-ESM** version 1.1.00p2¹ with a low-resolution configuration. Since the atmospheric pCO₂ levels are prescribed, terrestrial carbon cycle from the land component **JSBACH** and oceanic carbon cycle from **HAMOCC** do not interact (fig. 2.1). The full Earth System Model (**ESM**) [Giorgetta et al., 2013] as well as its components have been described and evaluated in detail by the given references. In the following subsections, I give an overview about the implemented processes affecting internal variability of the oceanic carbon cycle.

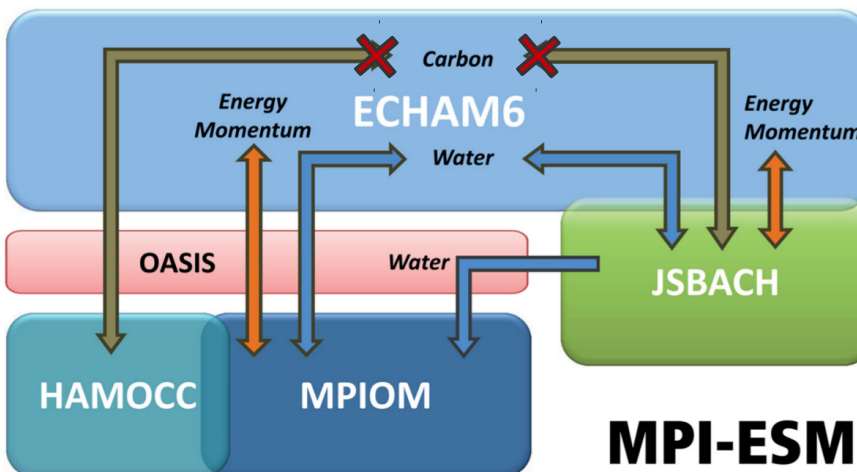


Figure 2.1: Schematic overview on the different components in **MPI-ESM** with prescribed atmospheric partial pressure pCO_{2,atm} [Giorgetta et al., 2013]

2.1.1 ECHAM

ECHAM is an general circulation model for the atmosphere. **ECHAM** has an sea-air gas exchange interface with **HAMOCC** and exchanges

¹ full source code: <https://code.zmaw.de/projects/mpi-esm/repository/show/tags/mpiesm-1.1.00p2>

water, energy and momentum with **MPIOM**. The atmosphere component **ECHAM**6.3 runs on a T63 grid, corresponding to 1.9° horizontal resolution, with 47 vertical layers up to 0.01 hPa [Stevens et al., 2013]. This high vertical resolution and atmospheric height allows to model jets which originate in the tropopause. Those jets define the position and strength of the westerly winds in the Southern hemisphere. Changes in **ECHAM** with regard to **CMIP5** version in Stevens et al., 2013 are described in Bittner et al., 2016. They majorly include the new radiation code of **ECHAM**6.3.

2.1.2 MPIOM

The Max Planck Institute Ocean Model (**MPIOM**) is an ocean general circulation model (OGCM) with a horizontal resolution of 1.5° on average on the Arakawa C-grid, 40 fixed-depth vertical levels on a realistic topography and with a free surface [Jungclaus et al., 2013]. The spatial resolution of 1.5° translated to a grid cell length of ~ 150 km at the northern edge of the Southern Ocean at 30°S and ~ 40 km in Antarctic coastal waters. Eddies are parametrized by the GM-scheme [Gent et al., 1995]. Therefore, the vertical mixing and diffusion based on Richardson-number dependent formulation is important for vertical gradients [Pacanowski and Philander, 1981]. Tracers are advected by the Navier-Stokes equations with Boussinesq-approximation.

The Mixed-Layer Depth (**MLD**) is calculated by a potential density criterion where the difference between the sea-surface density and the lower end of the mixed-layer is 0.125 kg m^{-3} [Jungclaus et al., 2013].

2.1.3 HAMOCC

The HAMBurg Ocean Carbon Cycle Model (**HAMOCC**) is a global marine carbon cycle model which simulates oceanic carbon and nutrient cycles [Maier-Reimer, 1984; Maier-Reimer, 1993; Six and Maier-Reimer, 1996]. As a subsystem in the ocean, biogeochemical tracers except for opal and calcite shells are advected by **MPIOM**. **HAMOCC** aims to reproduce distributions of biogeochemical parameters over various timescales from seasons to millenia without regional tuning or temporal adjustments towards observations [Ilyina et al., 2013]. This includes processes on three compartments: sea-air interaction at the sea surface, biogeochemistry of the water column and sediment biogeochemistry (fig. 2.2). The **HAMOCC** model version for the large ensemble is identical to the one used in **CMIP5** which is analyzed in detail in Ilyina et al., 2013. In the following subsection, I will only give an overview about the implementation of the most relevant processes for the variability on decadal and shorter timescales.

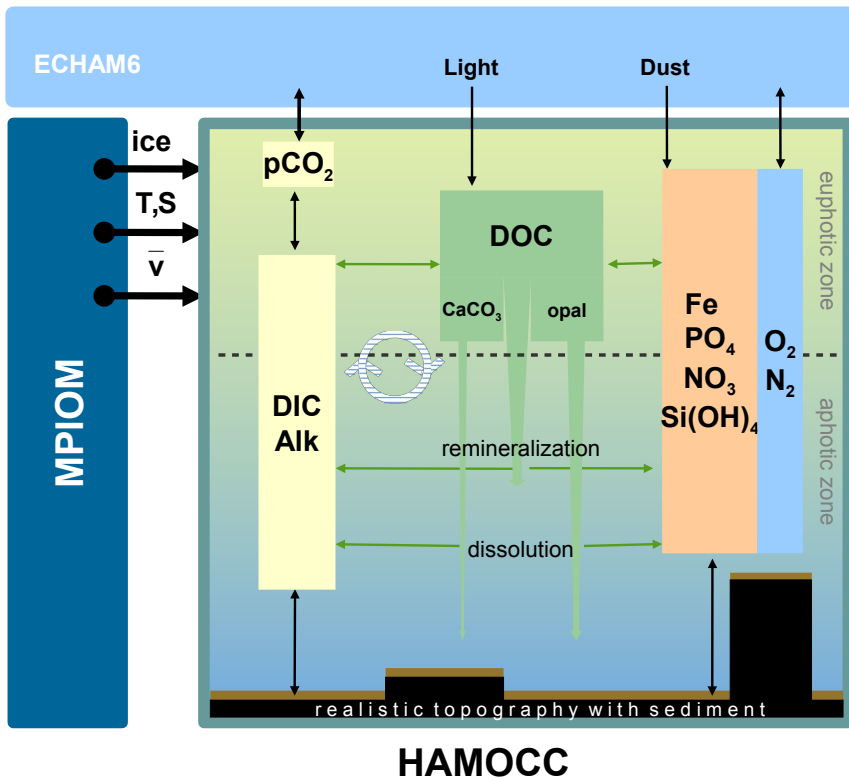


Figure 2.2: Schematic overview of the global ocean biogeochemistry model **HAMOCC** [Ilyina et al., 2013] which is coupled to the atmospheric model component **ECHAM** and the ocean model **MPIOM**. The ocean model provides state variables of physical oceanography, i.e. ice cover, temperature (T), salinity (S) and the advective velocities (\bar{v}). The water column holds tracers of gases, i.e. oxygen (O₂), nitrogen (N₂), laughing gas (N₂O), and dimethyl sulfide (DMS); nutrients, i.e. iron (Fe), phosphate (PO₄), nitrate (NO₃) and silicic acid Si(OH)₄; and tracers of carbonate chemistry, i.e. Dissolved Inorganic Carbon (DIC) and total alkalinity (Alk). Photosynthesis converts DIC and nutrients to Dissolved Organic Carbon (DOC), which produces calcium carbonate (CaCO₃) or opal shells.

The carbonate system determines pCO_{2,ocean} [Maier-Reimer, 1993]. Dissolved inorganic carbon and alkalinity are directly calculated as prognostic tracers from which other tracers derived. When pCO_{2,atm} reacts with seawater, the carbonate chemistry evaluates oceanic pCO_{2,ocean} based on the law of mass action formulae, which dependent on temperature (calculated according to Weiss, 1974), salinity, DIC and alkalinity.

The CO₂ flux calculation implemented in the model follows an empirical relationship under the conceptual one-layer ocean-sided stagnant film model with gas transfer velocity k_w [Wanninkhof, 1992]:

$$\text{CO}_2\text{flux} = (1 - f)k_w\Delta p\text{CO}_2$$

$$k_w = 0.31u_{10}^2(\text{Sc}(T)/660)^{-\frac{1}{2}}$$

$$\Delta p\text{CO}_2 = p\text{CO}_{2,\text{ocean}} - p\text{CO}_{2,\text{atm}},$$

where f is the sea-ice fraction of the grid cell, u_{10} is the wind speed at 10 m height, Sc is the temperature-dependent Schmidt number, 660 is the Schmidt number of CO₂ in seawater at 20°C, and $\Delta p\text{CO}_2$ is the difference between the partial pressure of CO₂ in the atmosphere and the ocean, so positive values of sea-air CO₂ flux represent a net flux from the ocean to the atmosphere.

In the euphotic zone upto a depth of 90m, phytoplankton converts inorganic nutrients, e.g. phosphate (PO₄), nitrate (NO₃), and iron (Fe), and DIC to organic matter by photosynthesis. The biological pump [Volk and Hoffert, 1985] is implemented based on an extended NPZD-type ecosystem formulation [Six and Maier-Reimer, 1996]. Phytoplankton growth is co-limited by nutrients (phosphate, nitrate and iron), temperature and light: Phytoplankton is parametrized by bulk phytoplankton, which mimics the combined growth of diatoms, coccolithophores and dinoflagellates under exponentially increasing optimum growth rate temperatures [Eppley, 1972]. Phytoplankton growth depends linearly on the availability of light, without saturation for stronger irradiance. The temperature-irradiance dependence is combined by a limitation function in Smith, 1936 (fig. A11). Michaelis-Menten kinetics describe the nutrient limitation of the maximum phytoplankton growth rate with a half-saturation constant [Michaelis and Menten, 1913]. The limiting role of nutrients is described by the nutrient availability factor that multiplies with the average growth rate of phytoplankton. The macro-nutrient iron is modeled by iron-relaxation from lignans. Iron enters the water column via a monthly dust input climatology, is used in photosynthesis and released in remineralization.

There are two different falling detritus: opal producing, if silicate is available or else calcium carbonate producing.

Once detritus reach the the ocean floor, particulate matter enters the sediment and finally the burial layer. At the upper boundary of the sediment, all tracers are in exchange with the sediment which via pore water exchange [Heinze et al., 1999].

2.2 LARGE ENSEMBLE SIMULATIONS

Large ensemble simulations are a novel tool to investigate model internal variability. "Climate variability refers to variations in the mean

state (...), which may be due to natural internal processes within the climate system (internal variability), or to variations in natural or anthropogenic external forcing (external variability)" [IPCC, 2013]. The variability in observations is impossible to separate, if - like in the case of pCO₂ no long-lasting direct measurement records exist. Although modeled internal variability is not equivalent to observed internal variability, we can learn about the random variations of natural processes.

By iterating a climate simulation with an identical forcing and model code but slightly perturbed initial conditions, single ensemble members will be exposed to the same process implementations. The interplay of those at stochastically random level lets each realization evolve in a unique way while still being bound to a common forced signal, which follows the external forcing. Perturbed initial conditions large ensemble simulations allow to distinguish a signal into a forced signal, which is the average signal across all ensemble members, and the residual, which modulates the signal around the forced signal due to internal variability [McKinley et al., 2016; McKinley et al., 2017]:

$$\text{signal} = \text{forced signal} + \text{internal variability}.$$

As running large ensembles simulation comes with high computational costs, this area of climate modeling research is still more recent. There are only a few datasets available and published papers are still rare, e. g. [Deser et al., 2012; Thompson et al., 2015; Lovenduski et al., 2016; Krumhardt et al., 2017; Kay et al., 2015; McKinley et al., 2016; Ilyina, 2016; Bittner et al., 2016; Hedemann et al., 2017; Rodgers et al., 2015].

The MPI-ESM LE contains 100 simulations under historical CMIP5 forcing from 1850 to 2005. The forcing includes volcano eruptions from the historical period and solar cycles. Anthropogenic forcings include well-mixed greenhouse gases, anthropogenic sulphate aerosols and land-use change. Atmospheric pCO₂ levels are prescribed according to the CMIP5 protocol [Taylor et al., 2012]. The carbon cycle is not coupled, so effects of changes in the terrestrial or oceanic carbon sink are not reflected in the atmospheric pCO_{2,atm}.

Ensemble members differ through starting from different year of the pre-industrial control simulation, so ocean and atmosphere have slightly different initial conditions in each run. This was achieved by branching off ensemble members from a 2000-year pre-industrial control run after roughly 50 years, when the historical forcing sets it.

NCAR's Community Earth System Model (CESM) LE [Kay et al., 2015] lead to the first studies of perturbed initial conditions large ensembles on internal variability by Deser et al., 2012. CESM LE served for studies analyzing the timescales of detection of trend in the ocean

carbon sink [McKinley et al., 2016] and the partitioning if its uncertainties [Lovenduski et al., 2016].

The initial state of the atmosphere was slightly perturbed by roundoff-level changes to air temperature in their 32 runs.

Geophysical Fluid Dynamics Laboratory ([GFDL](#)) ran a 30-member ensemble simulation based on their model ESM2M. They use different dates separated by one day each, but didn't publish any oceanic carbon uptake paper yet [Rodgers et al., 2015].

Although the initialization of ensembles differs, the variability after a few model years is not affected anymore by initialization method, but by model variability [Hawkins and Sutton, 2009].

CESM Large Ensemble studies like Deser et al., 2012 and Thompson et al., 2015 assume Gaussian statistics. In [sec. 2.4.3](#), I show that our larger ensemble generates spatial and temporal distributions with statistics similar to gaussian distributions assuming that variability does not change over this 25-yr period.

2.3 OBSERVATIONAL DATA

There are large uncertainties in observational-based CO₂ flux products, especially in the Southern Ocean [Rödenbeck et al., 2015]. Direct pCO₂ measurements in the Southern Ocean are sparse and discontinuous. Different mapping techniques lead to a spread in observation-based estimates.

For comparison of CO₂ flux with model simulations, I use the Self-Organizing Map-Feed-Forward Network ([SOM-FFN](#)) data which is based on the Surface Ocean Atlas ([SOCAT](#)) Version 2 [Bakker et al., 2014] since 1982. It uses a neural network-based data interpolation to create pCO₂ maps [Landschützer et al., 2013; Landschützer et al., 2014; Landschützer et al., 2016]. The data product is smoothed by a 3x3 filter averaging two months and the neighboring grid cells, but this has little effect on seasonal dynamics as this study focuses on the decadal variability. I use this pCO₂ data product because this method takes multiple variables for pCO₂ interpolation to cover regions without direct pCO₂ measurements. However, the input training data of the algorithm is seasonally biased, as the available pCO₂ samples originate mostly from austral summer months.

However, [SOM-FFN](#) as well as the mixed-layer scheme Jena-MLS [Rödenbeck et al., 2013; Rödenbeck et al., 2014] produces a relatively low monthly mismatch globally compared to original [SOCAT](#) data [Rödenbeck et al., 2015]. Both those data products agree on the decadal trends in the Southern Ocean. As the different data products cannot be validated or falsified, I use [SOM-FFN](#) as the best estimate - still acknowledging the current limitations of pCO₂ in-situ data.

2.4 STATISTICAL METHODS

2.4.1 Linear trends and statistical tests

The main tool for analysis - linear trends - is the computation of a linear regression coefficient via least-squares. With Student's t-test, I check in spatial patterns, whether this trend is significantly different to the null hypothesis (4) [Mood et al., 1974]. To exclude seasonal variability, the climatological seasonality is removed from all monthly data before trend computation.

The Mann-Kendall test is a statistical tool to assess if there is a monotonic upward or downward trend of the variable of interest over time [Mann, 1945; Kendall, 1975]. This test is applied in sec. 3.1 to extract trends based on a selection criterion of monotony.

Monotonic upward mean that it consistently increases over time. The Mann-Kendall test is best viewed as an exploratory analysis and is most appropriately used to identify stations where changes are significant or of large magnitude [Hirsch et al., 1982].

The Mann-Kendall statistic S counts magnitude relations of each pair of all available timesteps in a dataset with the sign function:

$$S = \sum \operatorname{sgn}(x_k - x_i).$$

This Mann-Kendall statistic S converts to probabilities for monotonic behavior according to Gilbert, 1987.

2.4.2 Choice of trends

To analyze the processes driving decadal internal variability σ_{DIV} (sec. 2.4.3), I focus on individual ensemble realizations in ch. 3 and 4. Here, I have to make a compromise between signal strength and robustness versus trend length. The longer a period, the more likely the trend deviates from a monotonic behavior, e.g. after a few years of monotonic increase the trend flips (fig. 3.2). Therefore longer trends show less chance to have a strong signal per trend-length (fig. A2). Also, longer trends experience a stronger influence of atmospheric forced trend. Furthermore, the underlying mechanisms for CO₂ flux trends in our ensemble simulation seem to be of the same origin regardless of the exact length of the trend period. Therefore, I decided to select 8-year trends in ch. 3 to understand the trending processes in ch. 4, because 8-year trends are still very close to a decadal 10-year trends and still able to show similar magnitude and monotonic behavior as the observation-based estimate. Monotonic behavior is maintained by a Mann-Kendall test above a probability threshold of 0.98 ($S_{\text{threshold}} \leq 16$), which does not require strictly monotonic behavior, but allows few deviations.

2.4.3 Decadal internal variability

Internal variability is present on many timescales. To investigate decadal internal variability, I assess the differences of the annual mean state in a decade. Therefore, I define decadal internal variability σ_{DIV} of any variable X as the standard deviation of the changes in M running multi-year (specifically 8-year) decades in all N ensembles:

$$\sigma_{DIV}(X) = \sqrt{\frac{1}{MN} \sum_{n=ens}^N \sum_{m=yr}^M (X_{m,n} - \bar{X}_{m,n})^2}$$

$$X_{m,n} = X_{\text{decade}_{\text{end},n}} - X_{\text{decade}_{\text{start},n}}$$

I use values of the annual values to filter out seasonal variability and set the turn of the year to the end of July to fully capture one austral summer season, which allows in-depth analysis for trends in biology.

Previous studies assume Gaussian statistics, but lack an adequate ensemble size to check for in detail [Deser et al., 2012; Thompson et al., 2015]. The Max Planck Institute-Earth System Model Large Ensemble (**MPI-ESM LE**) used for this study includes 100 members. Furthermore, I increases my sample size and calculate trends in running intervals between 1980 and 2004, so strictly speaking internal variability here is defined in ensemble space and temporal space, which should not differ much over this period of 25 years.

The temporal distribution of the spatially integrated sum of the Southern Ocean south of 35°S (fig. A1a) as well as of a single randomly chosen grid cell in the Southern Ocean CO₂ flux (fig. A1b) follow Gaussian statistics. Assuming this also for other variables allows me to use the standard deviation as a metric and interpret those as probabilities.

2.5 CLIMATOLOGICAL METHODS

2.5.1 Southern Annular Mode Index

The Southern Ocean westerly winds are variable in strength and location. To describe this variability the Southern Annular Mode (**SAM**) index was defined by Gong and Wang, 1999. To construct the index, I remove the climatological seasonal cycle from the maps of sea-level pressure and take a zonal mean of the latitudes 40°S and 65°S, standardize them against the climatological period of 1950-1979 as P^* and take the difference to create the index value:

$$SAM = P_{40^\circ S}^* - P_{65^\circ S}^*$$

2.5.2 Thermal separation

In order to separate the influence of temperature on CO₂ flux, I apply the methodology of Takahashi et al., 1993; Takahashi et al., 2002. The thermal component pCO_{2,thermal} to account for the effect of changes in Sea-Surface Temperature (SST) on pCO₂. The non-thermal component pCO_{2,non-thermal} approximately accounts for all other changes.

$$\begin{aligned} \text{pCO}_{2,\text{thermal}} &= \overline{\text{pCO}_2} \cdot \exp [0.0423^{\circ}\text{C}^{-1} (\bar{T} - T)] \\ \text{pCO}_{2,\text{non-thermal}} &= \text{pCO}_2 \cdot \exp [0.0423^{\circ}\text{C}^{-1} (\bar{T} - T)] \end{aligned}$$

The overbar indicates the temporal average.

3

MODEL EVALUATION IN THE SOUTHERN OCEAN

My analysis of the internal variability of the Southern Ocean carbon sink originates in the evaluation of air-sea CO₂ flux (sec. 3.1). As the strength of the CO₂ flux in the Southern Ocean is modulated by the strength of westerly winds [Lovenduski et al., 2007], I assess also the sea-level pressure field and winds (sec. 3.2), followed by its impact on biology (sec. 3.3) and upper-ocean circulation (sec. 3.4).

A previous model evaluation of HAMOCC for the Coupled Model Intercomparison Project 5 (CMIP5) provides a global view on biogeochemistry [Ilyina et al., 2013]. Here, I evaluate the model focusing on the Southern Ocean and specifically the processes related to the carbon sink. In each subsection, I compare the modeled mean state of the Southern Ocean to observational data and assess modeled decadal internal variability in spatial distribution and temporal evolution.

3.1 CO₂ FLUX

The patterns of CO₂ flux are mainly controlled by primary production (see in detail sec. 3.3) and water transport (see in detail sec. 3.4). Ekman suction, also referred to as upwelling, drives degassing and Ekman subduction, also referred to as downwelling, drives CO₂ uptake or ingassing. Positive values indicate outgassing and negative values CO₂ uptake by the oceans.

The climatological ensemble mean state from 1980 to 2004 of the Southern Ocean CO₂ flux in MPI-ESM marks the Antarctic coastal region as a CO₂ sink, whereas the upwelling waters at 50-60°S are outgassing regions in the Atlantic and Indian sector and CO₂ flux neutral in the Pacific (fig. 3.1a). North of 50°S, the oceans take up CO₂ because of stronger primary production and Ekman subduction.

SOM-FFN observational-based estimate data show similar patterns of carbon uptake and outgassing, but in lower absolute values (fig. 3.1c). Hardly any measurements in the region of seasonal ice cover make a comparison with observation-based values hard to interpret.

For spatial distributions, I define decadal internal variability σ_{DIV} as the standard deviation over the changes in decades in the whole ensemble (sec. 2.4.3).

The region 45-60°S is most variable. This is the area of Ekman suction (fig. 3.8a) and the southern edge of primary production area

(fig. 3.5a). The change in latitudinal position and strength of the westerly winds affects the position and amplitude of upwelling (sec. 3.4) and primary production (sec. 3.3).

The observation-based **SOM-FFN** decadal variability σ_{DIV} is most pronounced at 50-60°S in the Atlantic and Indian and south of 60°S in the Pacific [Landschützer et al., 2016]. The amplitude of decadal variability is smaller than in **MPI-ESM** (fig. 3.1d). However, this comparison is limited by large differences in sample size between the 22-year observational record and the 100 **MPI-ESM** realizations.

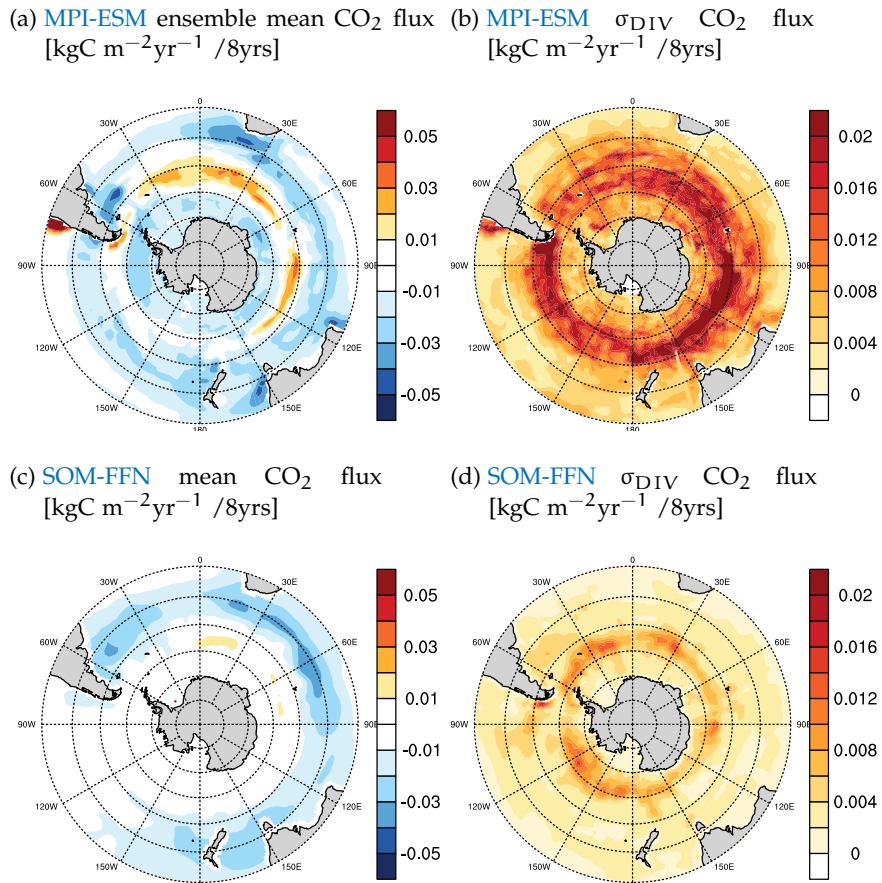


Figure 3.1: Spatial distribution of the climatology (a,c) and decadal internal variability σ_{DIV} (b,d) from 1980-2004 of the Southern Ocean sea-air CO₂ flux: (a) **MPI-ESM LE** ensemble mean as forced signal, (b) ensemble decadal standard deviation as decadal internal variability σ_{DIV} , (c) **SOM-FFN** climatology 1982-2004, (d) **SOM-FFN** decadal variability σ_{DIV} ; negative values indicate ocean uptake.

The modeled temporal evolution of the Southern Ocean ensemble mean CO₂ flux south of 35°S is dominated by the forced negative trend of rising atmospheric CO₂ concentrations (fig. 3.2). However, no individual realization follows the negative trend strictly monotonic -

they oscillate around the ensemble mean state triggered by internal variability. Exemplary, the most extreme monotonic positive and negative 8-year trend is highlighted. The modeled ensemble mean sea-air CO₂ flux over the historical period 1980-2004 is -1.15 PgC/yr and decadal internal variability σ_{DIV} is 0.22 PgC/yr, much larger than the forced signal CO₂ flux trend of 0.02 PgC/yr.

The observational-based estimate for the whole region south of 35°S shows a strong positive CO₂ flux trend in the 1990s [Le Quéré et al., 2007] and a strong negative CO₂ flux trend, reinvigorating the carbon sink in the 2000s [Landschützer et al., 2015] (fig. 3.2). The modeled σ_{DIV} is lower than of the decadal variations of SOM-FFN. This means that on a multi-year and decadal time-scale, SOM-FFN is twice as variable as MPI-ESM LE CO₂ flux, but this comparison must be ingested with caution as the influent datasets have large variations in time space.

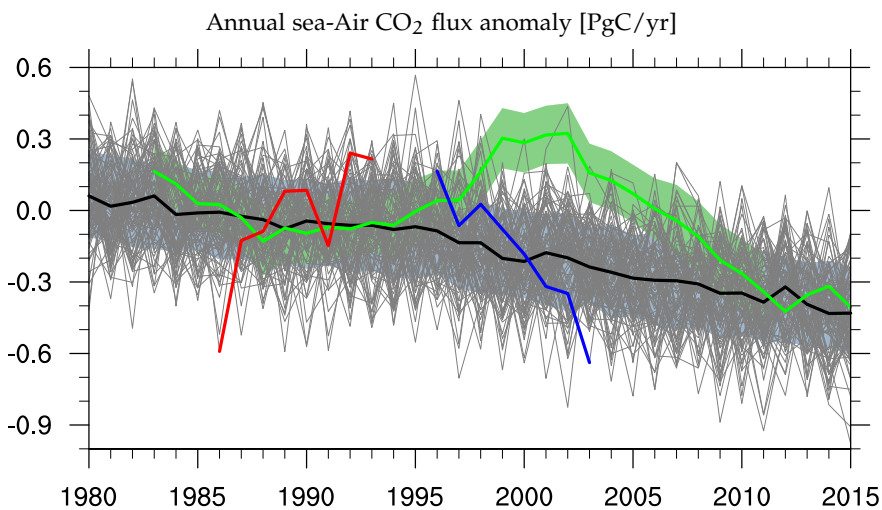


Figure 3.2: Temporal evolution of the Southern Ocean sea-air CO₂ flux anomaly south of 35°S with respect to the 1980s. Grey lines show the 100 ensemble members, the black line the ensemble mean, the blue shading is the ensemble decadal internal variability σ_{DIV} , the red line shows a positive CO₂ flux trend, the blue line shows a negative CO₂ flux trend, the green line represents the SOM-FFN observation-based estimate [Landschützer et al., 2015]; negative values indicate carbon uptake.

The decadal variability σ_{DIV} in SOM-FFN data is 0.35 PgC, with the most positive CO₂ flux trend in the 1990s of +0.40 PgC and the most negative trend of -0.72 PgC. Compared to SOM-FFN's σ_{DIV} , the magnitudes in observation-based trends could be due to internal variability with a probability of 70% ($\sim 1\sigma$) and $\sim 95\%$ ($\sim 2\sigma$) for 1990s and 2000s trends respectively. Under the context of MPI-ESM LE's σ_{DIV} , these magnitudes in observation-based trends could be due to internal variability with a probability of 5% ($\sim 2\sigma$) and 0.2% ($> 3\sigma$)

for 1990s and 2000s trends respectively. This outlines how unlikely these observed CO₂ flux trends can be attributed to internal variability from the perspective of numerical modeling.

The modeled internal variability of an interactive carbon cycle would be a more realistic counterpart for the observed internal variability, as the [MPI-ESM LE](#) simulations are forced with prescribed atmospheric CO₂ concentrations. The internal variability with an interactive carbon cycle produces 25% higher internal variability because of the non-linear changes in atmospheric CO₂ concentrations due to terrestrial carbon uptake [Ilyina et al., 2013].

Applying the selection criteria from [sec. 2.4.2](#), I focus on the two highlighted extreme CO₂ flux trends with monotonic behavior ([fig. 3.2](#)). Analyzing a range of trend lengths from 6 to 14 years, I assess that [MPI-ESM LE](#) is able to capture positive and negative multi-year and decadal CO₂ flux trends in the Southern Ocean ([fig. A2](#)). Monotonic multi-year (8-yr) trends reach up to $\sim 0.5 \text{ PgC/8yrs}$ and $\sim -0.6 \text{ PgC/8yrs}$. For decadal 10-year trends, the most extreme cases are of the same magnitude ($\sim 0.5 \text{ PgC/decade}$ and $\sim -0.7 \text{ PgC/decade}$) as those derived from observation-based estimates in the 1990s and 2000s [Le Quéré et al., 2007; Landschützer et al., 2015] ([fig. A2](#)).

3.2 WINDS

Winds are governed by distributions in Sea-Level Pressure ([SLP](#)). They point from high pressure to low pressure systems, but get diverted to their left in the Southern hemisphere by the Coriolis force. Therefore, strong westerly winds are established between the low-pressure system south of 45°S and higher pressure systems over the subtropical gyres ([fig. 3.3a](#)). This is zonally symmetric [SLP](#) pattern in the ensemble climatological mean leads to zonally symmetric westerly winds peaking at 50°S and decaying further northwards.

The spatial zonal distribution in observational data from a reanalysis climatology from National Centers for Environmental Prediction ([NCEP](#)) is so similar to the [MPI-ESM LE](#) climatology that I plot the difference between [MPI-ESM LE](#) climatology and [NCEP](#) reanalysis [Kalnay et al., 1996] ([fig. 3.3c](#)). The position of the jets in [ECHAM](#) is shifted to lower latitudes [Stevens et al., 2013] which seems to be a common atmospheric modeling challenge [Kidston and Gerber, 2010]. Therefore, the modeled westerlies are too strong from 30-60°S and too weak south of 60°S. The zonal wind speed difference peaks at 45°S at +1m/s.

The decadal internal variability σ_{DIV} increases zonally towards lower latitudes with the highest internal decadal variability in the pacific sector in the Southern Ocean seasonal ice-covered area ([fig. 3.3b](#)).

Observational reanalysis data reveal the same spatial distribution with a higher amplitude of decadal internal variability ([fig. 3.3d](#)). The pacific sector reflects the area of an Antarctic dipole induced from the El Niño-Southern Oscillation ([ENSO](#)), which manifests itself in variability of sea-ice [Yuan, 2004]. This is also known as the Pacific-South American (PSA) Oscillation [Sallée et al., 2008]. The atmospheric Southern Ocean jet splits and in El Niño conditions intensifies on a northern route which induces a low pressure system with more storms. La Niña conditions bring a high pressure system with less storms vice versa. Such tele-connections of the tropics into the Southern Ocean are subject of current research and rarely analyzed for the Southern Ocean carbon sink.

The temporal evolution and internal variability of the annual [SAM](#) index calculated according to [Gong and Wang, 1999] ([sec. 2.5.1](#)) is shown in [fig. 3.3](#). Positive [SAM](#) index values are associated with anomalously a low [SLP](#) over Antarctica which result in a southward shift and intensification of westerly winds. The [MPI-ESM](#) ensemble mean has a positive trend. This trend is a consequence to anthropogenic CO₂ emissions and ozone depletion over Antarctica [Thomp-

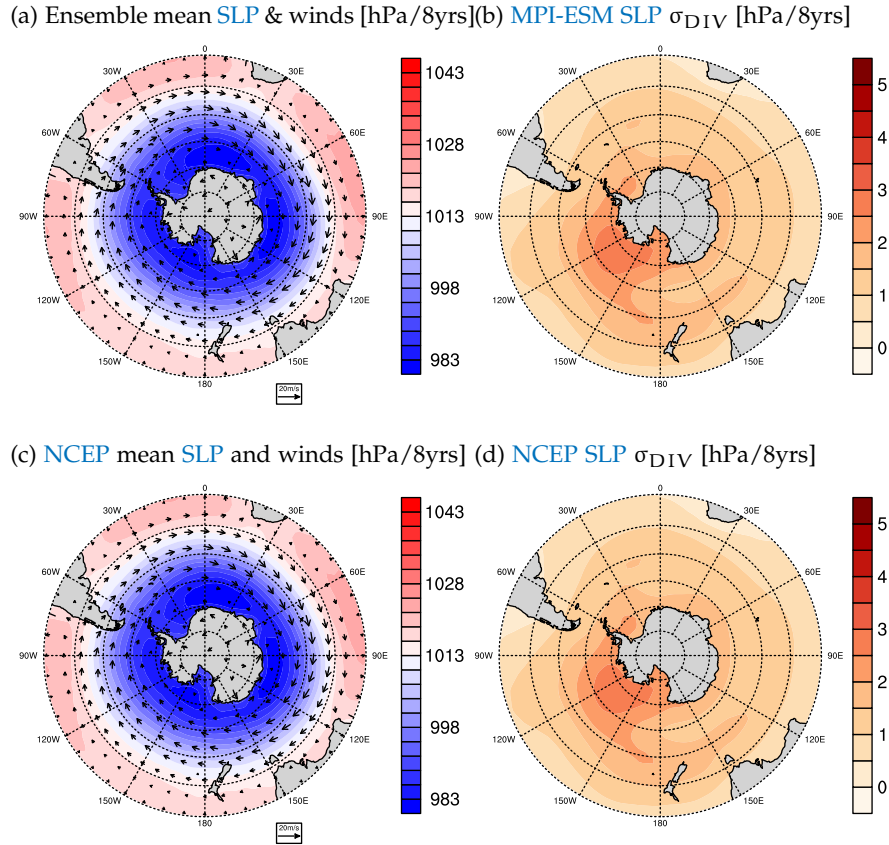


Figure 3.3: Spatial distribution of the Southern Ocean Sea-Level Pressure (**SLP**) and wind vectors overlain as arrows: (a) ensemble mean climatology from 1980 to 2004 as forced signal, (b) ensemble decadal standard deviation as decadal internal variability σ_{DIV} ; (c) difference between **MPI-ESM** and reanalysis data from **NCEP** reanalysis climatology [Kalnay et al., 1996], (d) decadal internal variability σ_{DIV} from **NCEP** reanalysis climatology.

son et al., 2011].

MPI-ESM LE SAM index lies in the range of the observational station-based **SAM** index from [Marshall, 2003], although it follows a weaker trend in the ensemble mean.

The positive CO₂ flux trend shows a positive trend in **SAM**. Those strengthening winds increase upwelling (sec. 3.4), which brings waters over-saturated in **DIC** to the surface and hence lead to outgassing anomalies. This weakens the carbon sink and vice versa strengthens the carbon sink under the context of weakening westerly winds. The detailed response of primary production and upwelling under the context of changing winds is discussed in ch. 4.

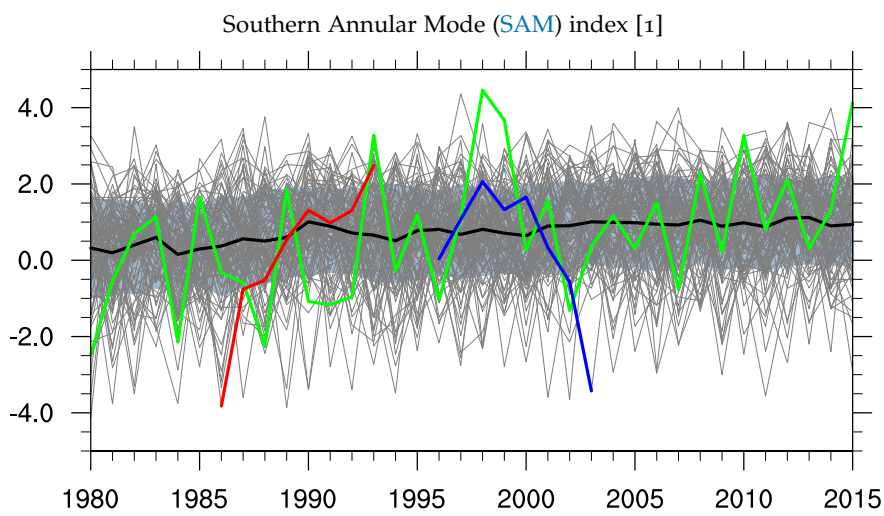


Figure 3.4: Temporal evolution of the annual Southern Annular Mode (SAM) index according to [Gong and Wang, 1999]. Grey lines show the 100 ensemble members; the black line the ensemble mean; the blue shading is the decadal internal variability σ_{DIV} ; the red line represents positive CO₂ flux trend; the blue line shows the negative CO₂ flux trend; the green line shows the station-based SAM from Marshall, 2003.

3.3 BIOLOGY

The strong seasonal cycle in insulation and the sparseness of land topography leads to first-order zonally symmetric constraints for light and SST. The high-latitude Southern Ocean is a so-called high nutrient low chlorophyll (HNLC) region, where light is the dominant limiting factor for the low biological production, but nutrients are plenty [Falkowski et al., 1998]. Summer sea-ice cover and sub-zero SST values constrain plankton growth and is responsible for the tiny amount of primary production in the coastal areas as well as the Ross Sea and Weddell Sea.

With decreasing latitude in the Southern Ocean, primary production increases along with increasing temperatures and light availability. Nutrients are upwelled by the upper-ocean overturning circulation and advected northwards by Ekman transport. This latitudinal increase of primary production peaks at 40-50°S, where nutrients are abundant from upwelling and Ekman transport and higher temperatures and light availability foster phytoplankton growth rates. The mixing with warm subtropical waters off the Argentinian coast increases SST and leads to a maximum primary production in the Southern Ocean [Behrenfeld, 2014]. Downstream the Drake passage, the polar front with its cold waters extends more northward [Orsi et al., 1995]. Along with lower nutrient concentrations due to increased precipitation from storms explains the relatively low primary production in the Atlantic sector compared to other longitudinal counterparts.

At the subtropical front, decreasing nutrient concentrations limit primary production [Behrenfeld, 2014].

To evaluate HAMOCC's ability to model the Southern Ocean, I do not compare modeled primary production to chlorophyll-a concentration derived from satellite data, because satellite images are frequently hidden by clouds. Instead, I compare the distributions of nitrate which is the limiting nutrient for biological production in this HAMOCC version. The distribution of nitrate shows a strong gradient in HAMOCC as well as in the World Ocean Atlas (WOA) 2013 [Garcia et al., 2013] along the fronts from high-nutrients in the high-latitudes to nutrient depletion in the subtropical gyres (fig. 3.6). In higher latitudes HAMOCC underestimates the phosphate concentration by 25%. These lower nutrient concentrations can be a sign of more nutrient consumption at higher primary production or be the reason for lower primary production. The distribution of another important nutrient phosphate shows a similar spatial pattern (??).

Internal decadal variability in vertically integrated primary production in the Southern Ocean is higher in high productivity areas

(fig. 3.5b). The whole region at 45-60°S, especially in the Indian sector, shows a enormously high decadal internal variability σ_{DIV} relative to the ensemble mean state. Internal variability in the Southern hemisphere is mostly driven by westerly winds. The explicit effect of those on HAMOCC is discussed in ch. 4.

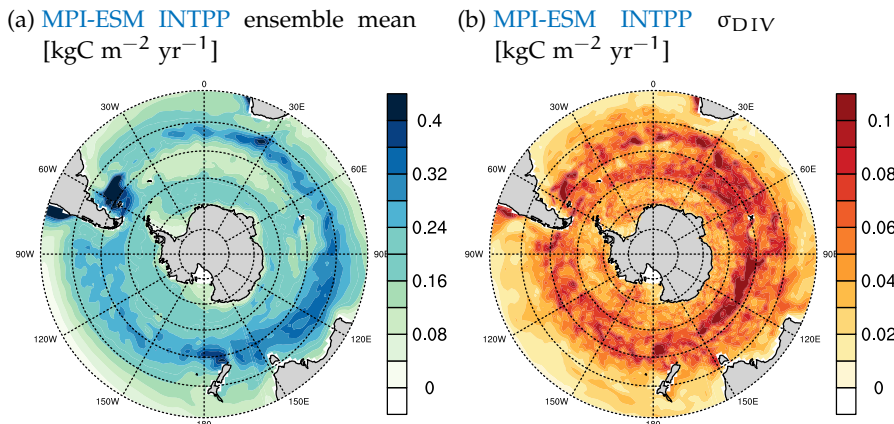


Figure 3.5: Spatial distribution of the vertically integrated primary production in the Southern Ocean: (a) climatological MPI-ESM ensemble mean from 1980 to 2004 as forced signal and (b) ensemble decadal anomaly standard deviation as decadal internal variability σ_{DIV}.

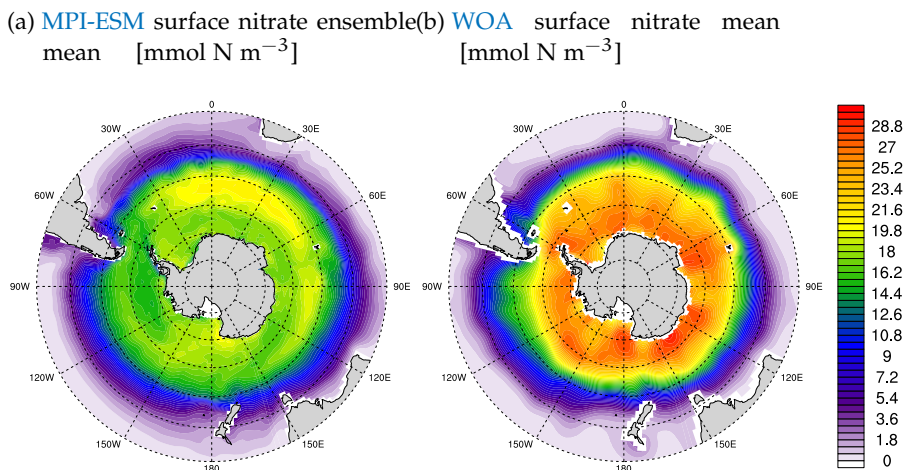


Figure 3.6: Spatial distribution of surface nitrate in the Southern Ocean: (a) MPI-ESM ensemble mean climatology, (b) World Ocean Atlas (WOA) climatology data [Garcia et al., 2013].

Primary production in the Southern Ocean is not subject to a strong forced trend in the historical period, but varies internally (fig. 3.7). The weak decreasing trend might be the first signs of increased stratification due to sea-surface warming, which in turn inhibits the mixing

of nutrients. But the long-term consequences for primary production is subject to ongoing research and debate [Bopp et al., 2013; Taucher and Oschlies, 2011; Lozier et al., 2011; Kessler and Tjiputra, 2016; Krumhardt et al., 2017; Deppeler and Davidson, 2017]. The decadal internal variability σ_{DIV} is 0.5 PgC.

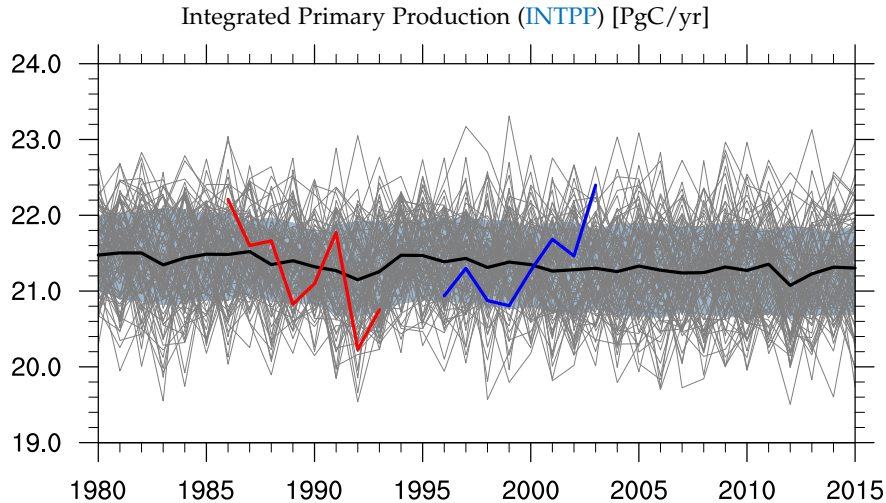


Figure 3.7: Temporal evolution of the Integrated Primary Production (INTPP) in the Southern Ocean south of 35°S. Grey lines show the 100 ensemble members, the black line the ensemble mean, the blue shading is the decadal internal variability σ_{DIV} , the red line represents the positive CO₂ flux trend, the blue line represents negative CO₂ flux trend.

The absolute amount of primary production exceeds CO₂ flux by a factor of ~20. The spatial distribution of export flux at 90m, which is the particulate organic matter that sinks below the euphotic zone before being remineralized, is the same as for primary production. As a lower vertical boundary for a upper-ocean carbon budget of the euphotic zone, export flux is of similar magnitude as CO₂ flux and thus comparable for a upper-ocean carbon budget (ch. 5).

The negative CO₂ flux trend has a positive trend in primary production, because primary production lowers surface DIC, pCO_{2,ocean} and hence reduces CO₂ uptake by the ocean; and vice versa negative trends in primary production lead to positive CO₂ flux trends.

MPI-ESM is able to model the general features of the Southern Ocean, such as the characteristics of a high nutrient low chlorophyll region [Bopp et al., 2013]. But compared to other models and observational data, the seasonal cycle of phytoplankton blooms is amplified and too early in the Southern Ocean [Bopp et al., 2013; Nevison et al., 2015; Nevison et al., 2016]. The reason of this is under current debate in the MPI biogeochemistry research group. It could involve

that the Southern Ocean in [MPI-ESM LE](#) run is not iron-limited, but while changing the dust input fields and the iron cycling constants leads to an iron-limited Southern Ocean the amplified seasonality is still present [private Communication, Irene Stemmler (MPI, Hamburg)]. Also a look into the grazing of zooplankton and its variable formulation might lead to a more realistic primary production seasonality. Furthermore, the atmospheric bias in westerly winds and the Southern Ocean warm bias [Jungclaus et al., [2013](#)] hinders sea-ice to propagate more extensively. A proper representation of Antarctic sea-ice would come along with a cooler, more stratified Southern Ocean which modulates primary production.

Additionally, the longest standing data records, which are on the northern hemisphere in Iceland [Six and Maier-Reimer, [1996](#)], are used for the tuning of free model parameters. Historically, the Southern Ocean has never been in the focus of [HAMOCC](#).

3.4 UPPER-OCEAN OVERTURNING CIRCULATION

The Southern Ocean upper-ocean overturning circulation is driven by the divergence at 40-60°S corresponding to strong westerly winds ([fig. 3.8a](#)). The isopycnals, which separate water masses, orient themselves at values from Sallée et al., [2013b](#), but are shifted to fit to typical depths, which is a common feature in water mass comparison as models have different density biases [Sallée et al., [2013b](#)]. In the high latitudes south of 50°S, Ekman pumping brings Circumpolar Deep Water (**CDW**) from the ocean interior to the surface. At the surface, these waters are transported to the north. At lower latitudes, the surface waters warm and evaporation increases, so relatively cold and low salinity waters known as Antarctic Intermediate Water (**AAIW**) slide below warmer and more saline Sub-Antarctic Mode Water (**SAMW**) to extend northwards at intermediate depth. This process is called downwelling or Ekman subduction.

The strong upper-ocean circulation features upwelling south of 50°S, northward transport at 40-60°S and downwelling at 30-40°S and is known as the Deacon cell [Döös and Webb, [1994](#); Speer et al., [2000](#)]. The upper-ocean overturning circulation is driven by the strength and positions of westerly winds. Upwelling steepens and downwelling straightens the isopycnals along which the water masses flow [Marshall and Speer, [2012](#)]. The internal variability in the horizontal processes at intermediate depth is lower than at the surface, because the influence of winds decays with depth. The decadal internal variability σ_{DIV} of vertical Ekman pumping and subduction is of similar magnitude at 200m and 1000m ([fig. 3.8](#)).

[Fig. 3.8a](#) is similar to DeVries et al., [2017](#), fig. 1, which uses observational data in an inverse model to demonstrate changes in upper-ocean overturning circulation. Due to different vertical velocity regimes, I choose different boundaries for the transport, which prevents me from quantitative comparisons. Nevertheless, data of DeVries et al., [2017](#), fig. 1 show the main characteristics of the Deacon cell and water transport of comparable magnitude as in [MPI-ESM LE](#).

How does the upper-ocean overturning circulation relate to the carbon cycle? The concentration of **DIC** in general increases with depth due to the biological pump and remineralization at depth. This is most clearly seen in the subtropics and blurred by processes of mixing at higher latitudes ([fig. 3.8](#)). Still, upwelled waters from the deep oceans have a high pCO₂ potential at which they would equilibrate when lifted to the surface, so the upwelling super-saturated waters in high latitude waters drives CO₂ outgassing and downwelling takes CO₂ equilibrated waters into the deeper ocean ([fig. 3.8b](#)) [Morrison

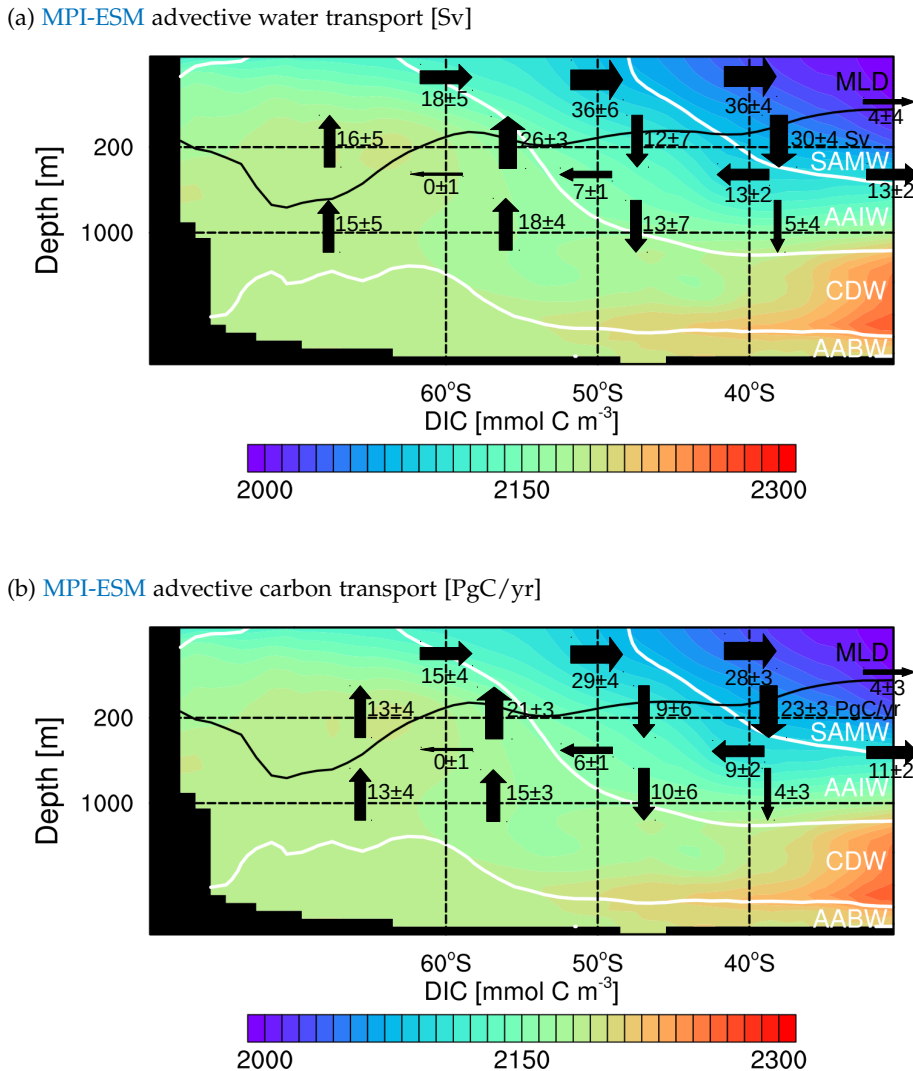


Figure 3.8: Zonally averaged transect of the Southern Ocean and the upper-ocean overturning circulation; black arrows show yearly mean advective transports of (a) water in Sv and (b) carbon in PgC/yr and the related decadal internal variability σ_{DIV} ; white lines are isopyncals separating SAMW at potential density $\rho_\theta = 1026.5 \text{ kg m}^{-3}$ from AAIW, at $\rho_\theta = 1027.2 \text{ kg m}^{-3}$ from CDW, at $\rho_\theta = 1027.7 \text{ kg m}^{-3}$ from AABW; the black line is the MLD; the colored contours show the distribution of concentration in DIC.

et al., 2015].

During the positive CO₂ flux trend upper-ocean overturning circulation intensifies. This means enhanced upwelling, which weakens the carbon sink (fig. 4.10) and vice versa strengthens the carbon sink for weaker upper-ocean overturning circulation (fig. 4.5).

The global performance of **MPIOM** is discussed in detail in Jungclaus et al., 2013. The Southern Ocean sea-surface temperature warm bias is attributed to an overestimation of downward shortwave radiation into the polar regions [Stevens et al., 2013] and causes the underestimation of sea-ice coverage. Additionally, through open-ocean convection in the Ross and Weddell Sea and deeper than observed winter mixing, heat from the relatively warm circumpolar deep waters warm the subsurface waters [Stössel et al., 2015]. Additional freshwater input from melting glaciers distributed along the coast a basal meltwater and along the high-latitude Southern Ocean to mimic freshwater input due to icebergs would improve the water column stability to prevent open-ocean convection. The same effect would have the coupling to a higher resolved atmosphere due to additional freshwater input [Stössel et al., 2015].

The model quality of overturning circulation in the Southern Ocean is analyzed by Sallée et al., 2013b. **MPI-ESM** realistically simulates subtropical water temperature and Sub-Antarctic Mode Water in general. But the overturning cell is much weaker than in other models.

The **MLD** is an important measure to assess how climate models represent the Southern Ocean. **MLD** in **MPI-ESM** is overestimated compared to observational data from **NOAA** Atlas [Monterey and Levitus, 1997]; in the locations of the Antarctic Circumpolar Current (**ACC**) and the Ross and Weddell Sea (fig. 3.9) as well as in the zonal average (fig. 3.8). In the Ross and Weddell Sea, the **MLD** deepens to few kilometers depth via open-ocean convection [Stössel et al., 2015], which often appears in climate models but rarely seen in observations [Heuzé et al., 2013; Lavergne et al., 2014]. This weak stratification explains why **MPI-ESM** overestimates **MLD** in winter [Sallée et al., 2013a].

(a) **MPI-ESM** MLD ensemble mean [m] (b) **NOAA** MLD Atlas mean [m]

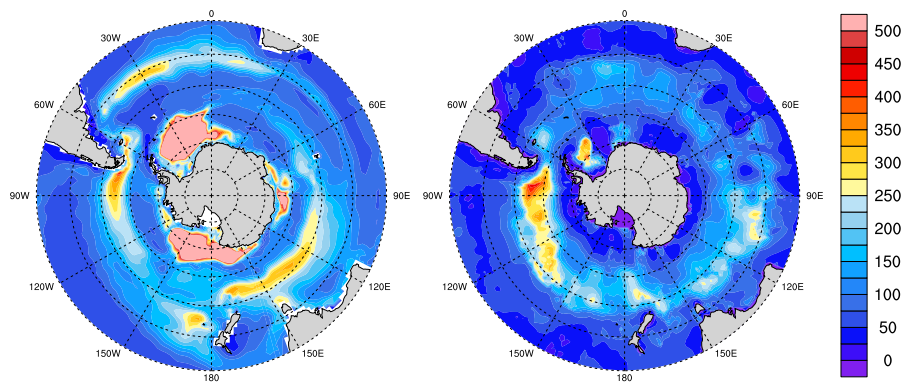


Figure 3.9: Spatial distribution of Mixed-Layer Depth (**MLD**) in the Southern Ocean: (a) **MPI-ESM** ensemble mean climatology, (b) **NOAA** Atlas climatology Monterey and Levitus, 1997.

4

PROCESSES CORRESPONDING TO MULTI-YEAR TRENDS IN SEA-AIR CO₂ FLUX

4.1 THE ROLE OF WESTERLY WINDS IN SOUTHERN OCEAN CO₂ FLUX VARIABILITY

Thompson and Wallace, 2000 and Hall and Visbeck, 2002 describe the Southern Annular Mode (SAM) as the most dominant mode for higher-latitude Southern Hemisphere variability. Lovenduski et al., 2007 explains the influence of the westerly winds on the Southern Ocean carbon sink.

To further assess internal variability due to westerly winds in MPI-ESM, this chapter discusses the effect of westerly winds on the physical and biological controls of the Southern Ocean carbon sink in HAMOCC.

I find a correlation on 8-year trends between SAM, which describes the position and latitudinal shift of westerly winds, and the CO₂ flux in the area of largest decadal internal variability at 50-60°S (fig. 4.1). Although the CO₂ flux formula (sec. 2.1.3) also depends on the wind speed at 10m height, the driver of the changes in fig. 4.1 is not the piston velocity k_w , but in Δp_{CO_2} [Lovenduski et al., 2015]. However, the magnitude of short-term variability on the timescale of days to hours depends highly on wind strength variability, but the direction of CO₂ flux is independent of wind speed. This relationship reveals two distinct regimes of wind-driven CO₂ flux signals in this area:

Intensified and southward shifted winds, associated with an increasing trend in SAM, lead to a positive CO₂ flux trend. This Southern Ocean carbon sink response has been suggested frequently for the observed and projected trend in SAM [Le Quéré et al., 2007; Lovenduski et al., 2007; Lovenduski et al., 2008; Hauck et al., 2013; Landschützer et al., 2015]. The related process responses associated with stronger winds are explained in sec. 4.2.

In MPI-ESM, I also find the reverse case of weakening and northward-shifting westerly winds, associated with a negative trend in SAM, which lead to a negative CO₂ flux or ocean uptake trend. The responses of processes associated with weaker winds are explained in sec. 4.3. However, observations do not reveal a strong multi-year negative SAM trend (fig. 3.4). Likewise, westerly winds did not weaken, but continued to increase during the negative CO₂ flux trend in the 2000s [Landschützer et al., 2015]. On the contrary, depending on the starting year of the trend period, the SAM index slightly weakened in the early 2000s [Marshall, 2003; Lovenduski et al., 2015], and also

DeVries et al., 2017 report a decline in upper-ocean overturning circulation which may be connected to strength and position of winds.

The strong trends originate in strong changes of the position and strength of Southern hemisphere westerly winds and effect of those on ocean circulation. However, the parametrized eddies in MPI-ESM LE might allow deeper mixing to sustain for multiple years and hence longer than the seasonal timescale at which the eddies would counteract those trends [Thompson et al., 2011]. Only a variable definition of isopyncal thickness diffusion could parametrize the expected eddy response from high-resolution simulations [Gent and Danabasoglu, 2011]. These enhanced eddy fluxes in a low-resolution model are discussed in Lovenduski et al., 2013.

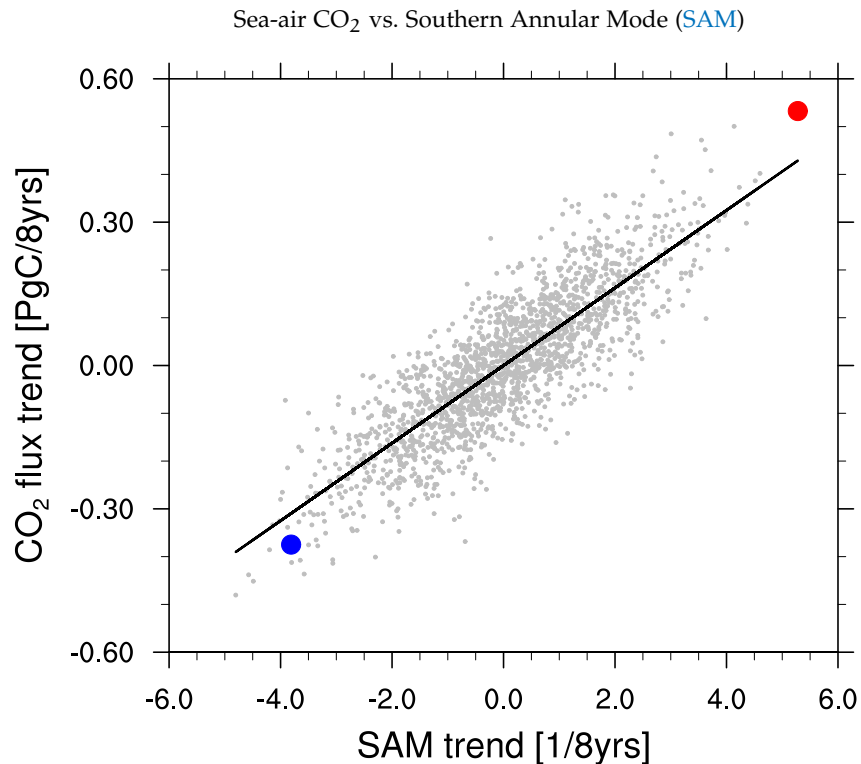


Figure 4.1: Linear trends in the [SAM](#) as indicator of wind strength vs. CO₂ flux at 50–60°S; each data point represents 8-year trends of a single realization normalized for the ensemble mean trend between 1980 and 2004; the blue dot is the most negative monotonic CO₂ flux trend; the red dot is positive monotonic CO₂ flux trend.

To qualitatively understand the mechanisms of the Southern Ocean carbon sink, I analyze the drivers of CO₂ flux on a process level. This chapter covers qualitative CO₂ flux changes with respect to the thermal effect, physical circulation and biology. A quantitative analysis of the different drivers for different regions follows in [ch. 5](#).

The analysis presented here involves 8-year trends for reasons stated in sec. 2.4.2, but the results of this chapter apply to various multi-year and decadal trends subject to internal variability (not shown).

The spatial trend patterns of different trend periods mostly appear zonally symmetric, therefore the analysis is not separated into the different Southern Ocean sectors, e. g. in the Pacific, Indian or Atlantic sector. Also, the atmospheric circulation change in MPI-ESM is too symmetric compared to observations [Haumann et al., 2014]. Therefore, the description here is carried out in zonal latitudinal bands keeping the unsymmetrical Southern Ocean dynamics in mind [Salée et al., 2010; Talley, 2013]. Also due to the underestimated Antarctic sea-ice and open-ocean convection in the Ross and Weddell Sea, I restrict my analysis to the Southern Ocean north of 60°S, but the decadal CO₂ flux trends have a weak signal south of 60°S anyway.

4.2 POSITIVE CO₂ FLUX TRENDS

Strong positive CO₂ flux trends correlate with stronger westerly winds (fig. 4.1) [Lovenduski et al., 2007]. The difference $\Delta p\text{CO}_2$ between oceanic pCO_{2,ocean} and atmospheric partial pressures pCO_{2,atm} depicts a cleaner signal than CO₂ flux (fig. 4.2a,4.2b) and is independent of wind speed and solubility [Lovenduski et al., 2015]. pCO_{2,ocean} rises stronger than pCO_{2,atm}, so CO₂ must be driven by changes in the ocean dynamics (fig. 4.2b). The strongest positive signal occurs in the upwelling at 50-60°S, a weaker and more patchy signal occurs in the subduction areas north of 50°S, whereas changes in most other areas of the Southern Ocean are insignificant (fig. 4.2b).

Westerly winds decrease at 40-50°S and increase at 50-60°S, which results in a southward shift of westerlies (fig. 4.2c) represented by the positive trend in SAM (fig. 3.4).

The response of the thermal effect, upper-ocean overturning circulation and biology are described in sec. 4.2.1, 4.2.2 and 4.2.3, respectively.

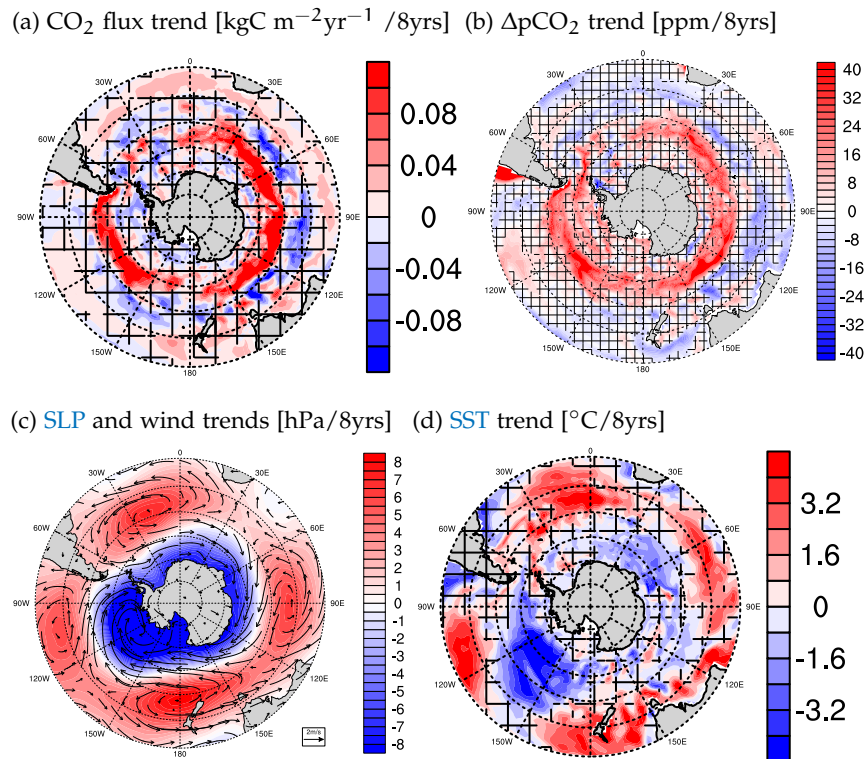


Figure 4.2: Linear trends in (a) sea-air CO₂ flux, (b) $\Delta p\text{CO}_2$, (c) SLP and wind vectors overlain as arrows and (d) Sea-Surface Temperature (SST) for the case of the most positive monotonic 8-year CO₂ flux trend; hatched areas indicate where trends are outside the 5% significance level.

4.2.1 Changes in the thermal effect during positive CO₂ flux trends

The solubility of pCO_{2,ocean} is primarily temperature sensitive. Warmer oceans such as the tropical oceans own a lower solubility than cooler high-latitude oceans - a process referred to as the solubility pump of carbon [Volk and Hoffert, 1985]. Likewise, CO₂-equilibrated waters outgas when warmed and take up CO₂ when cooled.

The difference between the partial pressure of CO₂ in oceanic pCO_{2,ocean} and atmospheric pCO_{2,atm} is the main changing quantity in the CO₂ flux formula [Lovenduski et al., 2015] (sec. 2.1.3). The separation by Takahashi et al., 1993, 2002 gives insights about the direct influence of SST (sec. 2.5.2). The thermal pCO₂ trend is driven by changes in SST (fig. 4.3a), whereas the non-thermal ΔpCO₂ trend approximately includes all other changes in pCO_{2,atm}, biology, alkalinity, assuming constant SST (fig. 4.3b). The thermal pCO₂ trend and non-thermal ΔpCO₂ trend approximately add up to the trends in pCO₂ [Landschützer et al., 2015].

The thermal trend follows the SST cooling trend (fig. 4.2d) south of 50°S towards negative CO₂ flux trends, whereas the warming north of 50°S favors outgassing. Increased Ekman transport causes this heat divergence in polar regions and a heat convergence at lower latitudes [Hall and Visbeck, 2002] (fig. 4.5). The non-thermal component strongly increases south of 50°S, so overall the pCO_{2,ocean} increases faster than pCO_{2,atm}, which leads to a positive CO₂. This reflects the enhanced outgassing from increased upwelling. The non-thermal and thermal trends combined nearly compensate north of 50°S, but at 50-60°S the outgassing dominates (fig. 4.2b). The homogeneous increase in atmospheric pCO_{2,atm} accounts for a -12 ppm/8yrs in ΔpCO₂ (fig. 4.2b). These changes are stronger in the summer season, especially the non-thermal component (fig. A7, A8).

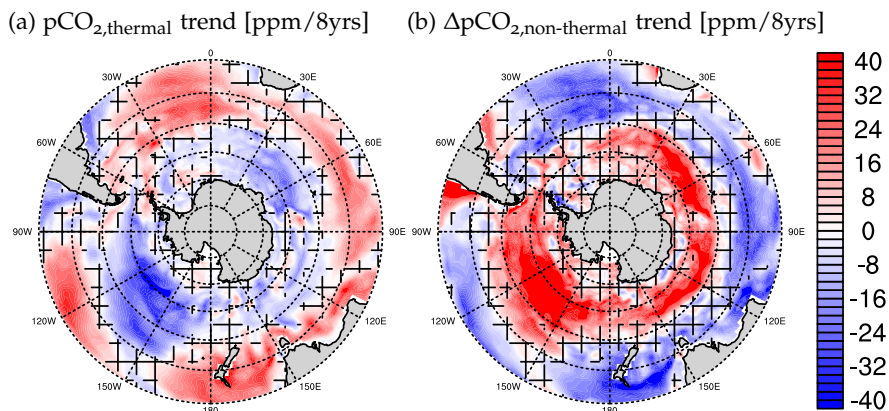


Figure 4.3: Linear trends in pCO_{2,thermal} (a) and ΔpCO_{2,non-thermal} (b) for the case of the most positive monotonic 8-year CO₂ flux trend; hatched areas indicate where trends are outside the 5% significance level.

4.2.2 Changes in ocean circulation during positive CO₂ flux trends

Stronger westerly winds intensify the upper-ocean overturning circulation [Lauderdale et al., 2013]. Therefore the circulation field advects more DIC and alkalinity along its overturning pathway (fig. 4.5). Intensified upwelling of super-saturated waters at 50-60°S increase DIC and alkalinity concentrations in the euphotic zone (fig. 4.4b). As the pCO_{2,ocean} sensitivity of DIC is large than for alkalinity, this likely enhances pCO_{2,ocean}, which leads to a positive CO₂ flux (for a detailed dicussion see ??). The stronger winds also increase Ekman northward transport and advects DIC and alkalinity further northward (fig. 4.4a). North of 50°S, subduction rates of AAIW and SAMW formation increase, so pCO_{2,atm}-equilibrated waters take additional anthropogenic carbon into the deeper ocean. The southward shift of westerly winds weakens the northern edge of Ekman transport at 30-40°S.

The changes in MLD also contribute to the vertical transport of carbon. By deeper mixing in winter, more carbon-rich waters are included into the MLD, which then serves as a larger super-saturated reservoir. MLD deepens south of 50°S and slightly shoals north of 45°S, whereas open-ocean convection causes the unrealistic zonal MLD averages below 300m south of 60°S (fig. 4.5) [Sallée et al., 2013a; Stössel et al., 2015].

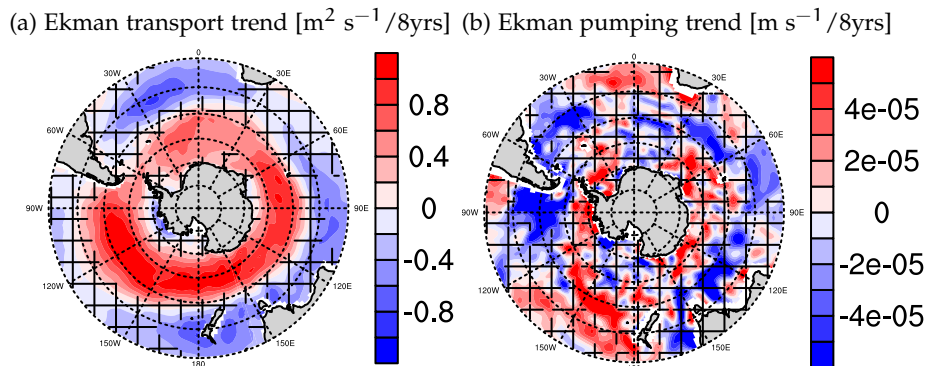


Figure 4.4: Linear trends in (a) Ekman transport and (b) Ekman pumping in the case of the most positive 8-years CO₂ flux trend; hatched areas indicate where trends are outside the 5% significance level.

The upper-ocean overturning circulation response presented here is in-line with idealized wind-change studies [Lauderdale et al., 2013], modeling studies explaining the observed CO₂ flux trend in the 1990s [Le Quéré et al., 2007; Lovenduski et al., 2007; Lovenduski et al., 2008], as well an inverse modeling study for the 1990s [DeVries et al., 2017].

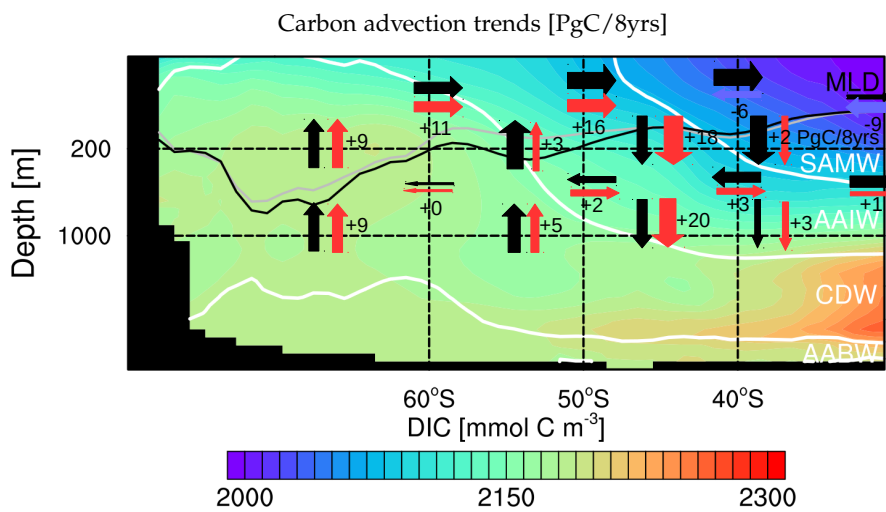


Figure 4.5: Zonally averaged upper-ocean overturning circulation in the case of the most positive 8-year CO₂ flux trend; black arrows show mean advective carbon transport, red arrows show advective carbon transport trends enforcing the upper-ocean overturning circulation; blue arrows show advective carbon transport trends weakening the upper-ocean overturning circulation; black numbers quantify the trends in advective carbon transport in PgC/8yrs; white lines are isopyncals as in fig. 3.8; grey line is MLD in the beginning and the black line MLD in the end of the period.

4.2.3 Changes in biology during positive CO₂ flux trends

The biological pump draws down surface Dissolved Inorganic Carbon (**DIC**), slightly increases alkalinity and is sensitive to changes in circulation (fig. A12). Mixing changes nutrient distributions, when remineralized nutrients from the deep ocean flush into the euphotic zone. Mixing also pulls the standing stock of phytoplankton deeper into the ocean, where less light inhibits growth. Changes in **SST** also directly affect phytoplankton growth (sec. 2.1.3).

In this subsection, I analyze the 8-year summer (SONDJF) austral summer trends to understand the trends in primary production.

Primary production and CO₂ flux show opposing zonally symmetric trend patterns as phytoplankton growth takes up large amounts of surface **DIC**, but only weakly increases alkalinity and hence lowers pCO₂ (fig. 4.2a, 4.6a). Primary production declines most pronounced at 50-60°S, increases at 40-50°S and declines at 30-40°S. Which changes drive these different responses?

Internally varying processes change the availability of nutrients. The decline in nutrients in the subtropics at 30-40°S reduces primary production, but the nutrient availability factor (sec. 2.1.3) slightly increases south of 50°S (fig. 4.6b). Previous observational and modeling studies suggest an increase in primary production, because upwelling brings nutrients, especially iron, from the deep-ocean to the iron-limited surface waters [Lovenduski and Gruber, 2005; Hauck et al., 2013; Wang and Moore, 2012; Tagliabue et al., 2014]. Additional iron fosters primary production following the iron-hypothesis [Martin et al., 1990; Martin, 1990], but observational data for iron is still rather sparse to test this for the whole Southern Ocean [Tagliabue et al., 2014]. Contrasting HAMOCC, many models reproduce this suggested iron-limitation in the Southern Ocean and hence respond with increasing primary production [Wang and Moore, 2012; Hauck et al., 2013].

If the reduction in primary production at 50-60°S cannot be explained by changes in nutrients, what else effects primary production blooms?

The combined light & temperature limitation is primarily driven by temperature after the insulation excels a threshold in cold waters (fig. A11). The strong **SST** cooling trend dominates the light & temperature limitation of primary production. The strong signal in coastal areas as well as Weddell and Ross Sea is attributed to sea-ice changes and open-ocean convection, but has minor effects on the primary production and CO₂ flux (fig. 4.6c).

This northward Ekman transport could also advect phytoplankton northwards to cause the increase in primary production at 40-50°S (fig. 4.4b, 4.6a).

The overall decline of primary production in the Southern Ocean under a positive SAM trend is related to mixing: The summer MLD has a strong increasing trend at 50-60°S, so the mixing deepens (fig. 4.6d). This is caused by stronger winds (fig. 4.2c) and shown in the average depth of the vertical diffusivity due to wind (fig. 4.6e). This deeper mixing in summer then mixes the standing stock of phytoplankton to deeper levels, where they are exposed to less light (fig. 4.6f) [Margalef, 1997]. This theory of a critical depth for phytoplankton blooms was initially proposed by Sverdrup, 1953 and requires a stable water column for phytoplankton to initiate blooms. However, this theory is based on turbulent mixing, so the oceanographic MLD only serves as a first-order mixing measure for phytoplankton [Franks, 2014]. Still the signal sustains to phytoplankton depth, where the average phytoplankton depth decreases up to 15m which results in up to 30% less light. The lack of monthly output for 3D biogeochemical variables made me use annual averages for phytoplankton, which causes the low significance in fig. 4.6f.

The reverse processes contributes to the increase at 40-50°S: Less winds mix less deep and allow phytoplankton to stay more confined to the surface, where they get more light and flourish (fig. 4.2c, 4.6e, 4.6f). Also the warming increases the phytoplankton growth rate (fig. 4.6c).

Summarizing, a multitude of interconnected processes causes the decline in primary production in the Southern Ocean for an increasing SAM trend. A clear separation of the magnitude of these interdependent processes is impossible.

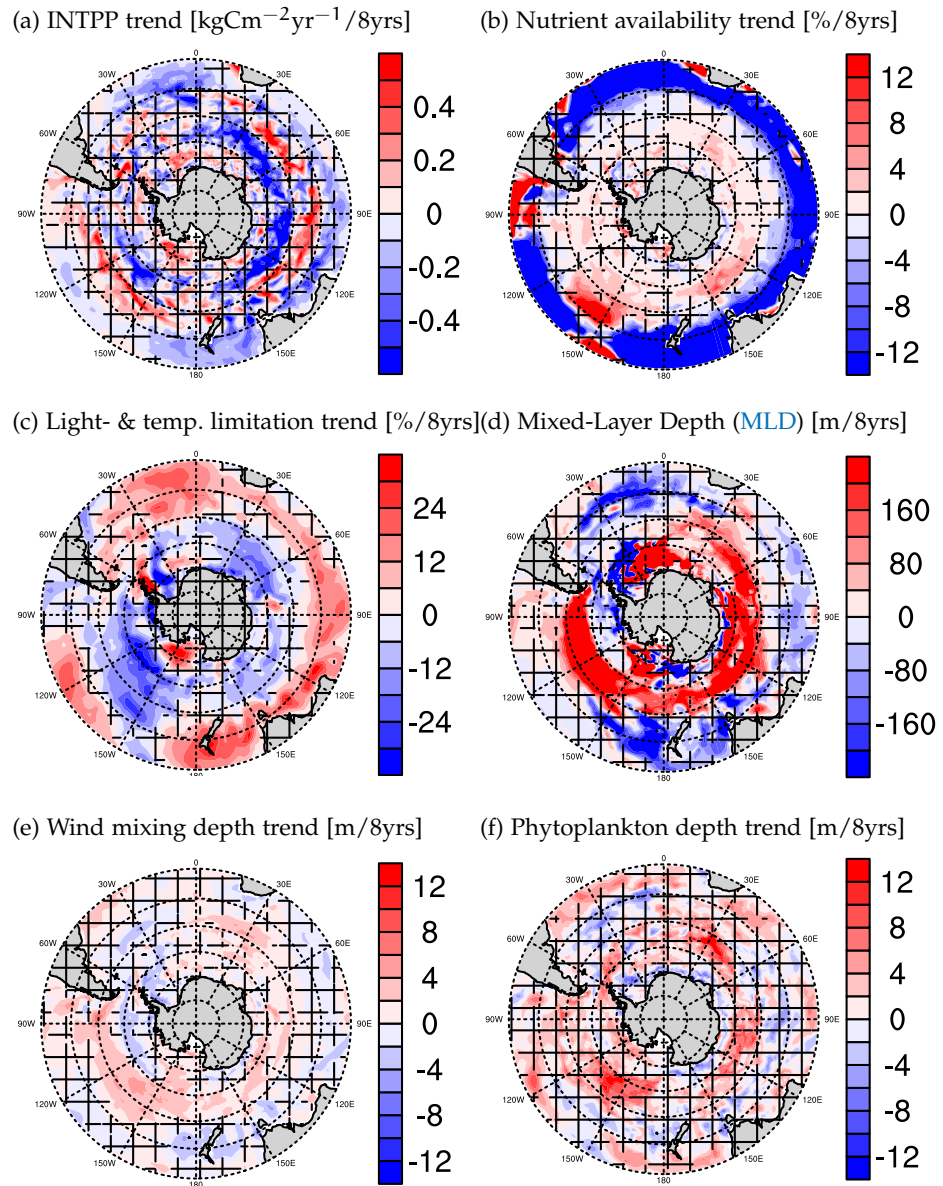


Figure 4.6: Southern Ocean austral summer trends for the most positive 8-year CO₂ flux trend: (a) Integrated Primary Production (INTPP), (b) nutrient availability factor, (c) surface temperature & limitation function, (d) Mixed-Layer Depth (MLD), (e) average depth of vertical diffusivity due to wind and (f) phytoplankton average depth; hatched areas indicate where trends are outside the 5% significance level.

4.3 NEGATIVE CO₂ FLUX TRENDS

Disclaimer: Generally in this analysis, the direction of trends reverse for weakening and northward shifting westerlies, which leads to an overall negative CO₂ flux trend. Additionally, now the prescribed atmospheric pCO_{2,atm} forcing promotes a steady negative background CO₂ flux trend.

A strong negative sea-air CO₂ flux trends correlates with weaker westerly winds ([fig. 4.7a, 4.7c](#)). The strongest negative signal ΔpCO₂ occurs in the upwelling area at 50-60°S. Changes in most other areas of the Southern Ocean are insignificant ([fig. 4.7b](#)).

The response in the thermal effect, upper-ocean overturning circulation and biology are described in [sec. 4.3.1, 4.3.2](#) and [4.3.3](#), respectively.

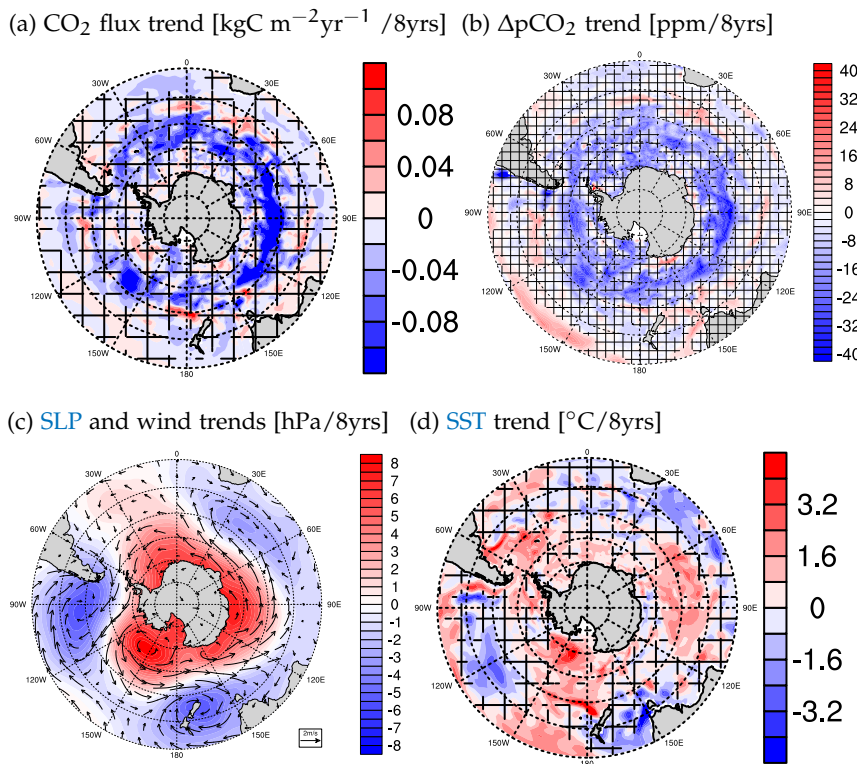


Figure 4.7: Linear trends in (a) sea-air CO₂ flux, (b) ΔpCO₂, (c) SLP and wind vectors overlain as arrows and (d) Sea-Surface Temperature (SST) for the case of the most negative monotonic 8-year CO₂ flux trend; hatched areas indicate where trends are outside the 5% significance level.

4.3.1 Changes in the thermal effect during negative CO₂ flux trends

The SST warming trend ([fig. 4.7d](#)) drives the thermal trend south of 50°S towards a positive pCO_{2,ocean} trend, whereas the cooling north of 50°S results in a pCO_{2,ocean} decline ([fig. 4.8a](#)). These SST changes are caused by less Ekman transport and lead to a heat convergence in the polar region and a heat divergence in the subtropics [Hall and Visbeck, [2002](#)]. The non-thermal trend has a strong negative signal south of 50°S and a slightly positive north of 50°S ([fig. 4.8b](#)). The increase in atmospheric pCO_{2,atm} accounts for a -14 ppm/8 yrs. The non-thermal and thermal trends combined nearly compensates north of 50°S, but the non-thermal component dominates at 50-60°S ([fig. 4.7b](#)).

These changes are stronger in the summer season, especially the non-thermal component ([fig. A9, A10](#)).

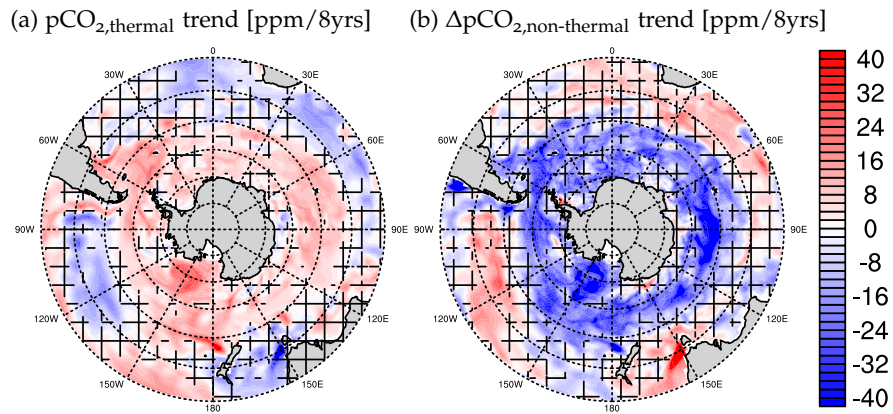


Figure 4.8: Linear trends in $p\text{CO}_{2,\text{thermal}}$ (a) and $\Delta p\text{CO}_{2,\text{non-thermal}}$ (b) for the case of the most negative monotonic 8-year CO₂ flux trend; hatched areas indicate where trends are outside the 5% significance level.

4.3.2 Changes in ocean circulation during negative CO₂ flux trends

Weaker westerly winds weaken the upper-ocean overturning circulation [Lauderdale et al., 2013], so the circulation field advects less DIC and alkalinity along its overturning pathway (fig. 4.10). Less upwelling at 50-60°S decreases DIC and alkalinity concentrations in the euphotic zone (fig. 4.9b). Weaker winds also decrease Ekman northward transport and reduces northward advection of DIC and alkalinity (fig. 4.9a). North of 50°S, subduction rates of AAIW and SAMW formation decrease, which could also be a sign of a northward-shift in upwelling. The MLD shoals south of 50°S and slightly deepens north of 45°S (fig. 4.10).

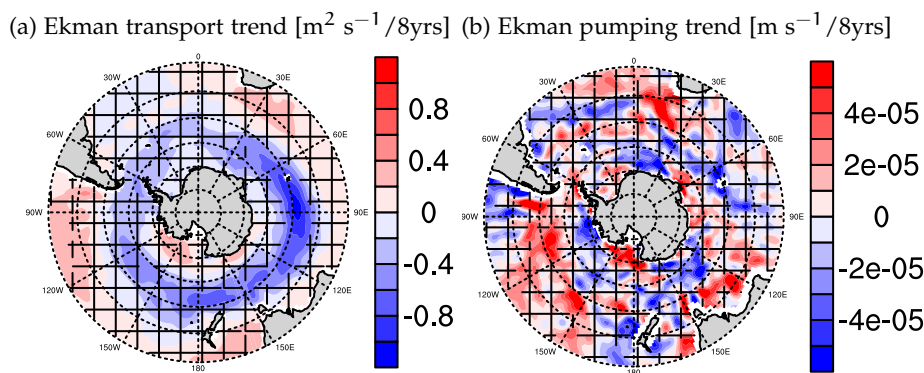


Figure 4.9: Linear trends in (a) Ekman transport and (b) Ekman pumping in the case of the most negative 8-years CO₂ flux trend; hatched areas indicate where trends are outside the 5% significance level.

This upper-ocean overturning circulation response agrees with idealized wind-change studies [Lauderdale et al., 2013]. The inverse modeling study reports a decline from the 2000s towards the previous decade [DeVries et al., 2017], which could be related to changes in wind. However, Landschützer et al., 2015 did not report a strong negative trend for the strength of observed westerly winds, but a pattern change in SLP in the 2000s became more zonally asymmetric. On the contrary, depending on the starting year of the trend period, the SAM index slightly weakened in the early 2000s [Marshall, 2003; Lovenduski et al., 2015].

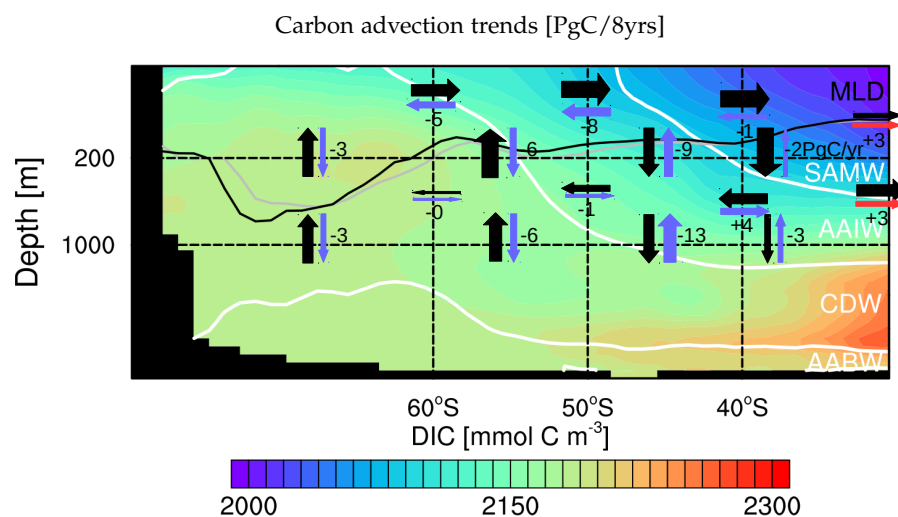


Figure 4.10: Zonally averaged upper-ocean overturning circulation in the case of the most negative 8-year CO₂ flux trend; black arrows show mean advective carbon transport, red arrows show advective carbon transport trends enforcing the upper-ocean overturning circulation; blue arrows show advective carbon transport trends weakening the upper-ocean overturning circulation; black numbers show the trends in advective carbon transport in PgC/8yrs; white lines are isopycnals as in fig. 3.8; grey line is MLD in the beginning and the black line MLD in the end of the period.

4.3.3 Changes in biology during negative CO₂ flux trends

Primary production and CO₂ flux show opposing zonally symmetric trend patterns ([fig. 4.7a](#), [4.11a](#)). The patchy trend patterns of primary production increase most dominant at 50-60°S, decrease at 40-50°S and increase at 30-40°S.

The additional supply of nutrients in the subtropics at 30-40°S fosters primary production, because the northward-shift in upwelling flushes nutrients from the deep into the nutrient-depleted subtropical gyre region. South of 45°S, the nutrient availability hardly changes and decreases ([fig. 4.11b](#)). Previous observational and modeling studies suggest an decrease in primary production because less upwelling brings less nutrients, especially iron, from the deep-ocean to the surface [Hauck et al., [2013](#); Tagliabue et al., [2014](#)]. But the Southern Ocean in [HAMOCC](#) is nitrate limited, so the slight reduction in nutrients rather originates in the increased nutrient consumption due to primary production.

The [SST](#) trends enhance primary production at 50-60°S and lower primary production north of 50°S ([fig. 4.11c](#)).

The weakened northward Ekman transport also keeps the standing stock more southwards and causes the increase in primary production at 50-60°S and the shifted decrease at 40-50°S ([fig. 4.9](#)).

Weaker winds mix the ocean less deep and thereby keeps the standing stock of phytoplankton in more light-flooded levels at 50-60°S ([fig. 4.11e](#)). The reverse process contributes to the decrease at 40-50°S.

Overall, primary production decreases for weaker and northward-shifting winds.

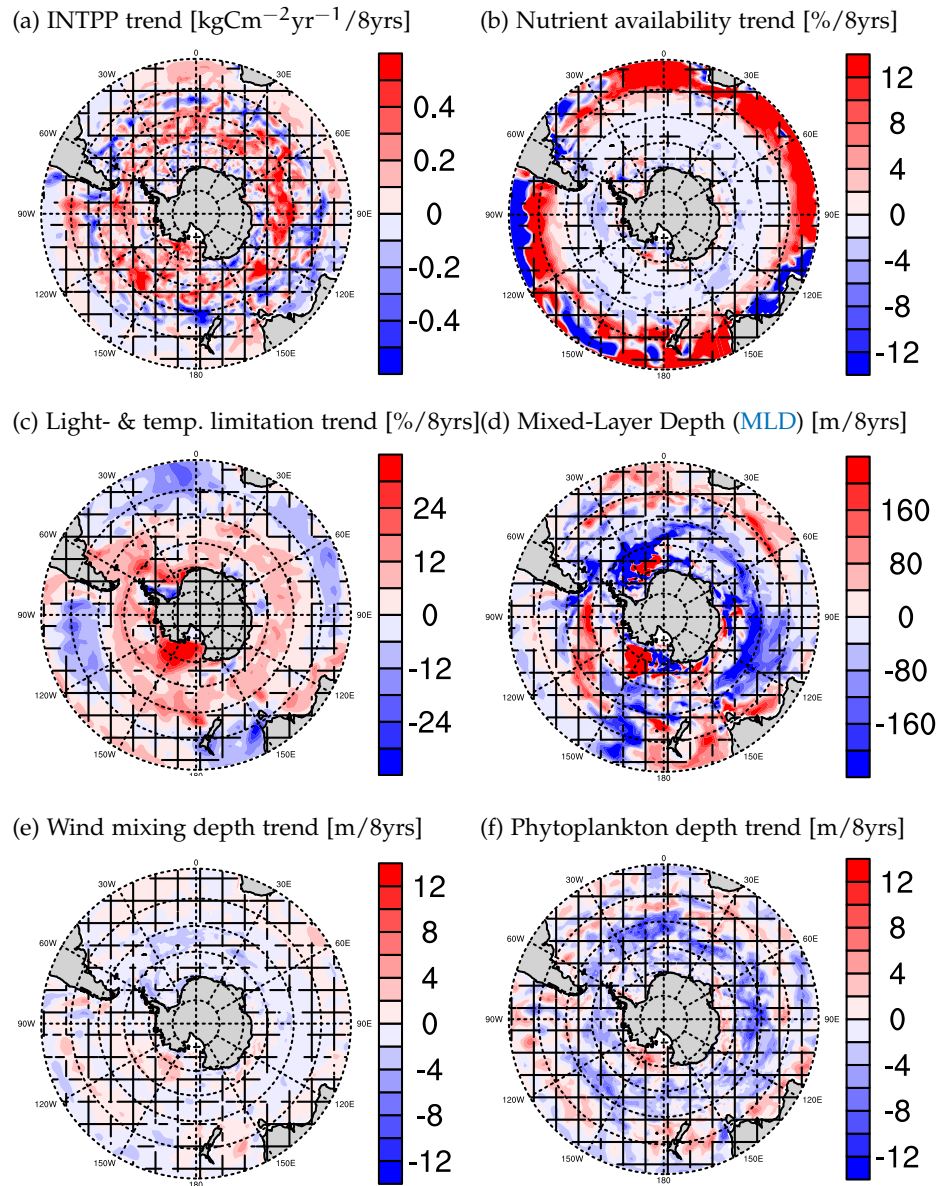


Figure 4.11: Southern Ocean austral summer trends for the most negative 8-year CO₂ flux trend: (a) vertically integrated primary production (INTPP), (b) nutrient availability factor, (c) surface temperature & limitation function, (d) Mixed-Layer Depth (MLD), (e) average depth of vertical diffusivity due to wind and (f) phytoplankton average depth; hatched areas indicate where trends are outside the 5% significance level.

CONTRIBUTION OF DIFFERENT PROCESSES TO MULTI-YEAR PCO₂ TRENDS

The previous analysis of thermal, circulation and biological responses to the westerly winds in ch. 4 asks for an estimate on the relative contributions of each process to the total change. As all the processes interact with each other, a clear and clean separation cannot be taken in precision. Therefore the results of this chapter must be understood rather as an *estimate of the first-order drivers* in pCO₂. In this chapter, I adapt the pCO₂ diagnostics framework from Loven-duski et al., 2007 to quantitatively estimate the different contributors to pCO_{2,ocean} and hence sea-air CO₂ flux changes.

5.1 DERIVATION OF THE FRAMEWORK

The framework relies on a well-mixed euphotic zone zonal carbon budget box (fig. 5.1). Based on the individual processes taking place, a change in pCO₂ due to that process is calculated from monthly model output data.

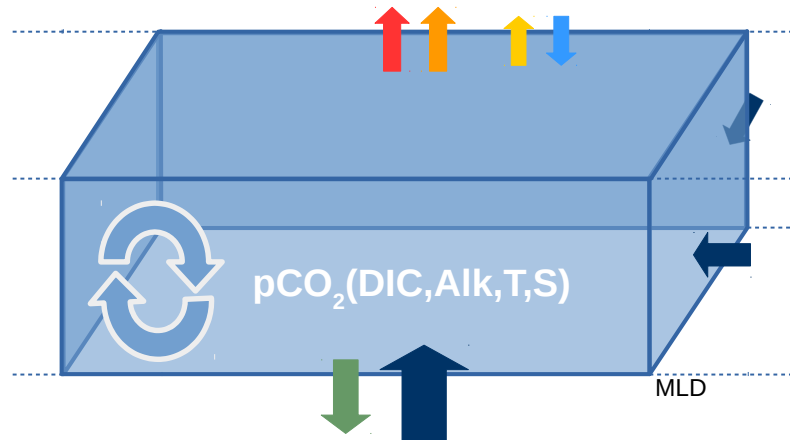


Figure 5.1: Schematic illustration of pCO₂ driver separation assuming a well-mixed zonal carbon box of the upper-ocean, where changes in pCO_{2,ocean} are separated into contributions due to sea-air CO₂ flux (red), thermal effect (orange), the saline effect (yellow), freshwater (light blue), biology (green) and a residual (dark blue)

I separate pCO₂ into different perspectives of understanding: The first view on the changes in dissociation constants separates contri-

butions in the thermal & saline effect and the second perspective regarding concentration changes in alkalinity (Alk) and DIC.

$$\delta pCO_{2,ocean} = \underbrace{\delta pCO_{2,thermal} + \delta pCO_{2,sal}}_{\text{dissociation constants changes}} + \underbrace{\delta pCO_{2,\text{non-thermal-sal}}}_{\text{concentration changes}}$$

$$\delta pCO_{2,\text{non-thermal-sal}} \approx \delta pCO_{2,Alk} + \delta pCO_{2,DIC}$$

The thermal separation from Takahashi et al., 1993; Takahashi et al., 2002 identifies a thermal pCO_{2,thermal} from pCO_{2,ocean}. This empirical thermal fitting function describes the changes in pCO_{2,ocean} of a warmed or heated water parcel, i. e. how the temperature-dependent equilibrium constants change the pCO_{2,ocean} at constant salinity, DIC and alkalinity. The salinity dependence for constant DIC and alkalinity describes the changes of dissociation constants due to changes in salinity, so an increase in salinity increases pCO_{2,ocean} [Sarmiento and Gruber, 2006], whereas the non-thermal-saline residual covers the changes of all other processes which vary pCO_{2,ocean} excluding the thermal and saline effect:

$$\delta pCO_{2,thermal} = \frac{\partial pCO_2}{\partial T} \cdot \delta T \approx \overline{pCO_2} \cdot 0.0423^{\circ}\text{C}^{-1} \cdot \delta T$$

$$\delta pCO_{2,sal} = \frac{\partial pCO_2}{\partial S} \cdot \delta S \approx \frac{\overline{pCO_2}}{\overline{S}} \cdot \underbrace{\gamma_S}_{\approx 1} \cdot \delta S$$

$$\delta pCO_{2,\text{non-thermal-sal}} = \delta pCO_{2,ocean} - \delta pCO_{2,thermal} - \delta pCO_{2,sal}$$

For a deeper look into the pCO_{2,ocean} due to concentration changes, I use the salinity-normalized concentrations ($sDIC = \frac{DIC}{S} \cdot S_0$, ($S_0 = 35$)) for DIC and alkalinity to prevent double-accounting of freshwater (FW) changes in DIC/alkalinity [Keeling et al., 2004]:

$$\delta pCO_{2,\text{non-thermal-sal}} \approx \frac{\partial pCO_2}{\partial (S/S_0 sAlk)} \delta(S/S_0 sAlk) + \frac{\partial pCO_2}{\partial (S/S_0 sDIC)} \delta(S/S_0 sDIC)$$

$$\approx \frac{S}{S_0} \frac{\partial pCO_2}{\partial Alk} \delta sAlk + \frac{S}{S_0} \frac{\partial pCO_2}{\partial DIC} \delta sDIC + \frac{\partial pCO_2}{\partial FW} \delta FW$$

The sensitivities of pCO_{2,ocean} to changes in DIC and alkalinity are taken from Sarmiento and Gruber, 2006:

$$\frac{\partial pCO_2}{\partial DIC} = \frac{pCO_2}{DIC} \cdot \gamma_{DIC}$$

$$\frac{\partial pCO_2}{\partial Alk} = \frac{pCO_2}{Alk} \cdot \gamma_{Alk}$$

Note the γ factors approximations, because they are partial derivatives from a simplified $p\text{CO}_{2,\text{ocean}}$ formulation Sarmiento and Gruber, 2006:

$$\gamma_{\text{DIC}} \approx \frac{3 \cdot \text{Alk} \cdot \text{DIC} - 2 \cdot \text{DIC}^2}{(2 \cdot \text{DIC} - \text{Alk})(\text{Alk} - \text{DIC})}$$

$$\gamma_{\text{Alk}} \approx -\frac{\text{Alk}^2}{(2 \cdot \text{DIC} - \text{Alk})(\text{Alk} - \text{DIC})}$$

Still, the characteristic properties of $p\text{CO}_{2,\text{ocean}}$ are preserved. $p\text{CO}_{2,\text{ocean}}$ increases for increasing **DIC** and decreases for increasing alkalinity.

Additional freshwater input reduces the concentration of **DIC**, alkalinity and salinity by dilution and leads to a slight decrease in $p\text{CO}_{2,\text{ocean}}$. Vice versa, net evaporation increases the concentration of **DIC**, alkalinity and salinity and thus increases $p\text{CO}_{2,\text{ocean}}$:

$$\frac{\partial p\text{CO}_2}{\partial \text{FW}} = \frac{s\text{DIC}}{S_0} \frac{\partial p\text{CO}_2}{\partial \text{DIC}} \delta S + \frac{s\text{Alk}}{S_0} \frac{\partial p\text{CO}_2}{\partial \text{Alk}} \delta S$$

Furthermore the changes in $s\text{DIC}$ and $s\text{Alk}$ are separated into biological, sea-air exchange and residual contribution to check for the origin of **DIC** and alkalinity changes, i. e. biological export, sea-air CO_2 flux or other not specified processes (likewise for $\delta s\text{Alk}$):

$$\frac{\delta(s\text{DIC})}{\delta t} = \frac{\delta(\text{DIC}_{\text{bio}})}{\delta t} + \frac{\delta(\text{DIC}_{\text{exchange}})}{\delta t} + \frac{\delta(s\text{DIC}_{\text{res}})}{\delta t}$$

The changes due to sea-air CO_2 flux and biology are converted to **DIC** and alkalinity concentration changes by dividing by the **MLD** assuming that the changes are well-mixed across the **MLD**. This assumes that the system is in a steady state and only changes in CO_2 flux, biological export and the residual affect the $p\text{CO}_{2,\text{ocean}}$ trend.

Furthermore, the concentration change of biological primary production and remineralization contributes with organic matter export (coex) and calcium carbonate export (caex) to changes in **DIC** and alkalinity. While both biological production processes reduce **DIC** by one unit, organic matter production increases alkalinity whereas calcification reduces alkalinity by two units. The magnitude of conversion factors arise from converting carbon to phosphate units in which alkalinity is accounted for. For a representation of the $p\text{CO}_{2,\text{ocean}}$ responses of the different processes see [fig. A12](#).

$$\delta\text{DIC}_{\text{bio}} = -\frac{\text{coex} + \text{caex}}{\text{MLD}}$$

$$\delta\text{Alk}_{\text{bio}} = -\frac{2 \cdot \text{caex} - 16/122 \cdot \text{coex}}{\text{MLD}}$$

Sea-air CO₂ flux reduces the **DIC** concentration without changing alkalinity:

$$\delta\text{DIC}_{\text{ex}} = -\frac{\text{CO}_2 \text{flux}}{\text{MLD}}$$

$$\delta\text{Alk}_{\text{ex}} = 0$$

These concentration changes in **DIC** and alkalinity modify pCO_{2,ocean} separately by different γ factors. These quasi-changes in **DIC** pCO_{2,DIC,bio} and alkalinity pCO_{2,Alk,bio} then add up the change due to biology pCO_{2,bio}.

The remaining salinity-corrected residual $\delta s\text{DIC}_{\text{res}}$ accounts for all other processes not covered in this framework and approximative errors:

- vertical and lateral advection of Dissolved Inorganic Carbon (**DIC**) and alkalinity
- changes in biological carbon inventory
- lateral advection of **DOC**
- linearizations of non-linear processes
- calculation from monthly timesteps
- simplifications of buffering constants in Sarmiento and Gruber, 2006

5.2 ESTIMATE OF PCO₂ DRIVERS

Applying the above described framework yields an estimate for the drivers of pCO₂ for the two extreme trends into the two latitudinal regions each with opposing responses from ch. 4 (tab. 5.1). In this section I analyze the pCO_{2,ocean} trends first under the perspective of dissociation constants changes, and then under the perspective of concentration changes to gain further insights on the non-thermal-saline part and frame a concluding picture of Δ pCO₂ and hence sea-air CO₂ flux.

pCO _{2,x} [ppm]	8-yr trend		50-60°S		40-50°S	
	positive	negative	positive	negative	positive	negative
pCO _{2,thermal}	-7.1	6.7	3.4	0.7		
pCO _{2,sal}	0.6	-0.5	0.2	-0.3		
pCO _{2,non-thermal-sal}	38.4	-8.7	6.4	12.5		
pCO _{2,FW}	0.6	-0.5	0.2	-0.3		
pCO _{2,sDIC}	37.6	1.0	10.6	19.1		
pCO _{2,sAlk}	8.1	-4.2	-1.8	-1.5		
pCO _{2,ex,DIC}	-5.1	5.2	0.2	1.1		
pCO _{2,bio,DIC}	5.5	-6.9	-1.5	-0.1		
pCO _{2,bio,Alk}	0.5	-0.6	-0.1	-0.0		
pCO _{2,bio}	6.0	-7.5	-1.6	-0.1		
pCO _{2,res,sDIC}	40.0	-0.8	9.8	18.2		
pCO _{2,res,sAlk}	7.8	-3.9	-1.7	-1.5		
pCO _{2,res}	47.8	-4.7	8.1	16.7		
pCO _{2,ocean}	32.1	-2.4	9.4	12.9		
pCO _{2,atm}	12.0	14.5	12.0	14.5		
dpCO ₂	20.2	-16.9	-2.6	-1.6		

Table 5.1: Trends in drivers of pCO₂ for the most extreme positive CO₂ flux trend and the most extreme negative CO₂ flux trend in two 10°-MLD boxes

During the most positive sea-air CO₂ flux trend at 50-60°S, the thermal trend pCO_{2,thermal} decreased because of sea-surface cooling and drives carbon uptake (sec. 4.2.1). While salinity changes are negligible, the overall trend opposes the thermal trend and is not caused by changes in dissociation constants in the thermal and saline effect, but in concentration changes.

A look in the processes changing DIC and alkalinity reveals that concentration of DIC and alkalinity has only a minor effect (fig. A12) and the largest contribution to the trends arises from the changes

in salinity-normalized alkalinity and mostly **DIC**. As outgassing increases (uptake decreases, sea-air CO₂ flux increases), **DIC** relatively increasingly leaves the upper-ocean box and thereby decreases pCO_{2,ocean}. For biological processes I take only the summer trends as inactive in winter. It comprises mostly organic matter production, which decreases and therefore exports less carbon and more alkalinity out of the system, which increases pCO_{2,ocean} ([sec. 4.2.3](#)). The remaining residual in **DIC** and alkalinity-driven pCO_{2,ocean} trends, which are not covered by a distinct process in this framework, dominate this concentration-driven pCO_{2,ocean} trend. Therefore in this instance, biology plays only a minor role and is likely outplayed by circulation changes. The changes due to upwelling are very dependent on the history of the water masses advected into and out of the system. Generally, deeper waters have higher **DIC** and alkalinity concentrations, where **DIC** would have a slightly higher impact on pCO_{2,ocean} because of slightly higher γ_{DIC} , but the proportions of **DIC** and alkalinity matter. So here, a strong **DIC** increase and alkalinity reduction are unaccounted for. This reflects either those properties related to advection changes or an underestimation of the organic matter production decrease. The trends in advection of both **DIC** and alkalinity are negative, so a clear attribution to upwelling cannot be made here ([sec. 4.2.2](#)).

At 40-50°S, the warming trend increases pCO_{2,thermal}, which drives CO₂ outgassing ([sec. 4.2.1](#)). Also the contributions unrelated to dissociation constants changes increase pCO_{2,ocean}, but at a higher rate.

Looking into these, biology slightly increases and lowers pCO_{2,ocean} ([sec. 4.2.3](#)), while changes in air-sea CO₂ flux are negligible. Overall the residual dominates again. Here, unaccounted increases in **DIC** and alkalinity overall increase pCO_{2,ocean}. As advection increases **DIC** and alkalinity this related to the circulation changes ([sec. 4.2.2](#)).

Combining the three distinct pCO₂ responses for the most extreme positive CO₂ flux trend from section [4.2](#) with the atmospheric pCO_{2,atm} changes leads to a comprehensive CO₂ flux picture ([fig. 5.2](#)).

While the cooling effect of the stronger winds reduces outgassing in the high-latitude Southern Ocean, the decline in primary production and mostly the increasing upwelling of carbon-rich waters and outplay the thermal effect to a strong relative outgassing pCO_{2,ocean} trend at 50-60°S. At 40-50°S the warming effect reduces carbon uptake, which is overtrumped non-thermal-saline changes, namely increasing **DIC** due to lateral advection and less downwelling (with negligible contributions from sea-air CO₂ flux and biology), which leads to a combined outgassing pCO_{2,ocean} trend.

The atmospheric trend pCO_{2,atm} is strictly positive and sets $\Delta p\text{CO}_2$ to a still strong positive trend at 50-60°S and a weak decreasing trend

at 40-50°S. The resulting outgassing CO₂ flux trend at 50-60°S is stronger than the weak CO₂ uptake trend at 40-50°S and hence determines the overall Southern Ocean carbon sink trend. The overall positive CO₂ flux trend and its opposite thermal contribution agrees with Lovenduski et al., 2007.

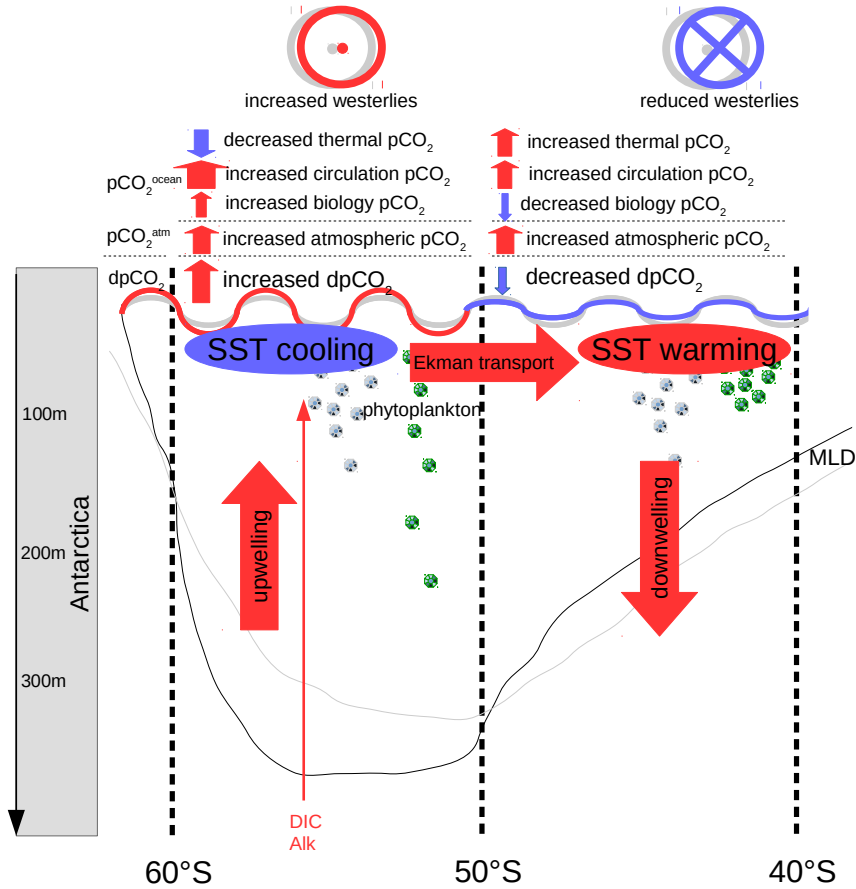


Figure 5.2: Schematic illustration of the Southern Ocean under the context of increasing westerly winds and response in the thermal effect, biology and upper-ocean circulation leading towards a positive CO₂ flux trend; red color-coding indicates a relative increase of the related quantity or process, whereas blue indicates a relative decrease. Stronger winds enhance the upper-ocean overturning circulation. Increased upwelling increases outgassing of over-saturated deep waters. Increased Ekman transport advects DIC further north, cools the higher latitudes and warms the lower latitudes. Deeper mixing and cooling in the higher latitudes decreases primary production, whereas shallower mixing and warming increase primary production in the lower latitudes. Combined with increasing atmospheric pCO₂, the higher latitude outgas strongly, whereas the lower-latitudes slightly ingas.

During the most negative sea-air CO₂ flux trend at 50-60°S, the thermal trend pCO_{2,thermal} decreased due to warming (sec. 4.3.1), but the thermal and saline effects are overcompensated by concentration changing processes, but of far less extent than for the most positive sea-air CO₂ flux trend, as the overall pCO_{2,ocean} has a slightly decreasing trend. The pCO_{2,ocean} change due in DIC increase only slightly, whereas the contribution from alkalinity dominates the negative trend. Looking into the individual processes, increased CO₂ uptake increases pCO_{2,ocean}, whereas increased biology reduces pCO_{2,ocean}. The residual DIC contribution slightly decreases as does DIC advection (sec. 4.2.2). The residual alkalinity contribution decreases stronger and seems to dominate this concentration-change-driven pCO_{2,ocean} trend, but the concentration changes in alkalinity due to advection also decline, so a clean attribution to advective circulation changes cannot be made here.

At 40-50°S, the thermal trend remains nearly unchanged and slightly warms (check sec. 4.3.1). The major trend in pCO_{2,ocean} outgassing arises from concentration changes.

Changes in DIC strongly lead this pCO_{2,ocean} outgassing trend by a strong residual DIC increase, which comes from increased DIC concentration due to advection, namely less northward advection and reduced downwelling. This reduced downwelling may be a sign increased upwelling caused by the northward shift of the overturning cell over the 40°S boundary. The same applies for increased alkalinity, which reduces pCO_{2,ocean} slightly.

The three distinct pCO₂ responses for the most extreme negative CO₂ flux trend from section 4.3 merge with the rising atmospheric pCO_{2,atm} into the opposing picture in CO₂ flux as for decreasing westerly winds (fig. 5.3).

Weaker winds warm the high-latitude Southern Ocean, which leads to outgassing, but the decreasing upwelling and the decline in primary production outplay the thermal effect to a relative ingassing trend at 50-60°S. At 40-50°S temperatures remain constant decreased Ekman transport DIC supply and increased northward-shifted upwelling leads to a combined relative pCO_{2,ocean} outgassing trend.

The strictly positive atmospheric trend pCO_{2,atm} outperforms the slightly pCO_{2,ocean} outgassing trend at 50-60°S and slightly overcompensates the pCO_{2,ocean} outgassing trend at 40-50°S. The resulting negative sea-air CO₂ flux signal at 50-60°S is stronger than the slightly positive sea-air CO₂ flux at 40-50°S and hence determines the overall Southern Ocean carbon sink trend.

The system is very susceptible in the magnitude of individual contributions for the definition of the depth of mixing, i.e. whether I choose the top layer of $\approx 12\text{m}$, fixed 90m , or actually taken vary-

ing depth as the Mixed-Layer Depth ([MLD](#)). The direction of the described processes and their relative contributions do not change and the residual adjusts accordingly.

The changes in inventory related to biology makes upto ~10% of the biological pCO_{2,ocean} change, but cannot be quantified correctly as the fraction of calcifiers is unknown.

The attribution of the residual changes in [DIC](#) to advective changes works at 40-50°S, but lacks the clear link at 50-60°S. The trends in alkalinity transport are close to the trends in [DIC](#) transport (as in [fig. 4.5](#) and [fig. 4.10](#)). Therefore, the pCO_{2,ocean} trends in the same direction cannot be explained entirely by advective circulation changes.

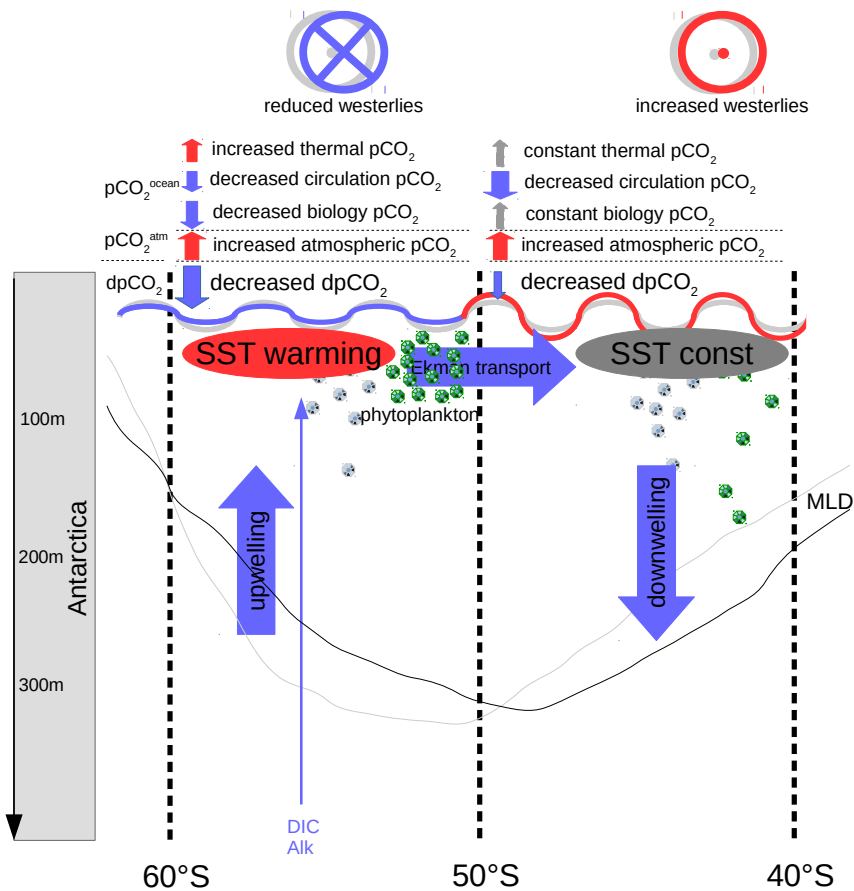


Figure 5.3: Schematic illustration of the Southern Ocean under the context of decreasing westerly winds and response in the thermal effect, biology and upper-ocean circulation leading towards a negative CO₂ flux trend; red color-coding indicates a relative increase of the related quantity or process, whereas blue indicates a relative decrease. Weaker and northward-shifted winds decrease the upper-ocean overturning circulation, increase primary production at higher latitudes because of deeper mixing and warming. Decreased Ekman transport warms the higher latitudes and reduces Ekman advection, but northward-shifted upwelling increases. Combined with rising atmospheric pCO₂, the higher latitudes strongly ingas, whereas the lower-latitudes slight ingas.

6

CONCLUSIONS AND OUTLOOK

To assess Southern Ocean CO₂ flux decadal internal variability, I analyze 100 historical Max Planck Institute-Earth System Model ([MPI-ESM LE](#)) simulations in the historical period from 1980 to 2004, for which the observational sea-air CO₂ flux product Self-Organizing Map-Feed-Forward Network ([SOM-FFN](#)) is available. I conclude this thesis by revisiting the research questions posed in the introduction.

What is the modeled internal variability of the Southern Ocean carbon sink?

I estimate the modeled decadal internal variability $\sigma_{\text{DIV}} = 0.22 \text{ PgC/yr}$ ([fig. 3.2, A1a](#)). Compared to the average 1980-2004 CO₂ flux south of 35°S of 1.15 PgC/yr, decadal internal variability σ_{DIV} amounts to 15% of the absolute Southern Ocean carbon sink. Internal variations dominates over the forced signal of 0.02 PgC/yr by one order of magnitude and hence is crucial in understanding changes in the Southern Ocean carbon sink. The area at 50-60°S hold the largest decadal variability ([fig. 3.1b](#)) and dominates the overall Southern Ocean CO₂ flux trend ([ch. 4](#)). [MPI-ESM LE](#) contains decadal trends of sea-air CO₂ flux upto ~0.5 PgC/decade and ~-0.7 PgC/decade - the same magnitude but less monotonic as suggested by observations [Landschützer et al., 2015] ([fig. A2](#)). Looking on the multi-year (8-yr) time scale, trends of ~0.5 PgC/8yrs and ~-0.6 PgC/8yrs show the same monotonic behaviour.

What are the sources of internal variability?

Sources of internal variability are the origins which trigger the thermal, physical and biological internally varying responses in CO₂ flux. The major source is the variability in strength and position of westerly winds in two distinct wind-driven regimes in the area of largest variability ([fig. 4.1](#)):

On the one hand, stronger and southward shifting westerly winds associated with a positive trend in the Southern Annular Mode ([SAM](#)) reduce the Southern Ocean carbon sink. On the other hand, weakening and northward shifted westerly winds leads to an increase in the Southern Ocean carbon sink.

What are the contributions of different processes to multi-year trends in sea-air CO₂ flux?

The increasing atmospheric pCO_{2,atm} drives all sea-air CO₂ flux trends alike to a more CO₂ uptake state, whereas the oceanic pCO_{2,ocean} is susceptible to internally varying processes:

For intensifying and southward shifting westerly winds, Sea-Surface Temperature ([SST](#)) cooling drives pCO_{2,ocean} decrease ([sec. 4.2.1](#)). Cooling and deeper wind-mixing reduce primary production, which increases pCO_{2,ocean} ([sec. 4.2.3](#)). These responses are dominated by a process that cannot be accounted for directly and is likely the increased upper-ocean overturning circulation, which enhances outgassing of deep waters and overall weakens the Southern Ocean carbon sink (summarizing [fig. 5.2](#)).

Vice versa, for weaker and northward shifting westerly winds the trends in the different processes reverse and likely decreasing upwelling and increased primary production result in an increase in the Southern Ocean carbon sink (summarizing [fig. 5.3](#)).

What do we learn from this large ensemble simulation about the Southern Ocean carbon sink?

While [MPI-ESM LE](#) does not aim to reproduce CO₂ flux trends suggested by observations in the first place, but it proves perturbed initial conditions large ensemble simulations are capable of capturing decadal internal variations similar to observations; even if this only applies for the most extreme decadal trends.

Forcing [MPI-ESM](#) with a historical CO₂ emissions instead of prescribed pCO_{2,atm} increases internal variability of the global carbon sink by 25% [[Ilyina et al., 2013](#)]. Therefore, internal variability with a fully coupled carbon cycle for the Southern Ocean carbon sink could have an even higher σ_{DIV} .

The strong trends discussed in this thesis originate in strong changes of the position and strength of Southern hemisphere westerly winds and effect of those on ocean circulation. However, the parametrized eddies in [MPI-ESM LE](#) might allow deeper mixing to sustain on longer time-scales than the seasonal timescale at which the eddies would counteract those trends [[Thompson et al., 2011](#)]. The impact of eddies on the carbon cycle in high-resolution simulations, especially in the Southern Ocean, is under current research [[Ito et al., 2010](#); [Dufour et al., 2013](#); [Gnanadesikan et al., 2015](#); [Meredith, 2016](#)]. Only a variable definition of isopycnal thickness diffusion could parametrize the expected eddy response from high-resolution simulations [[Gent and Danabasoglu, 2011](#)]. [Lovenduski et al., 2013](#) reproduces these increase eddy fluxes and the response to the carbon cycle, but the

general challenge of differing ocean circulation patterns remains and makes a comparison between a high-resolution resolved eddies and low-resolution parametrized eddies impossible [Bryan et al., 2014]. This effect of eddies asks for new low-resolution ensemble with variable isopycnal thickness diffusion or for high-resolution perturbed initial conditions large ensemble simulations.

The history of large ensemble simulations with perturbed large initial conditions is fairly recent. The attempt to study internal variability with [MPI-ESM LE](#) gives first insights into internal variability from many realizations of simulations. Understanding internal varying processes in our climate system might become increasingly important in the case of global CO₂ emission reductions, when the CO₂ reduction efforts are tracked by measurements and evaluated by scientists and politicians [Hawkins and Sutton, 2009; Lovenduski et al., 2016; Marotzke et al., 2017]. A further interesting project would be the comparison of different perturbed initial conditions large ensembles based on different models, i. e. comparing [CESM LE](#), [GFDL LE](#) and [MPI-ESM LE](#).

Climate models can only be as good as our current understanding of the climate system. For the Southern Ocean, however, there is a desperate need for an increasing amount of measurements to understand the Southern Ocean dynamics and biogeochemical properties. The recent ARGO data and the newly deployed biogeochemical floats currently advance the basis for understanding in the Southern Ocean. Elevating numbers of in-situ measurements help to overcome the current challenges in Southern Ocean modelling [Sallée et al., 2013a; Sallée et al., 2013b; Jungclaus et al., 2013; Lavergne et al., 2014; Haumann et al., 2014; Stössel et al., 2015; Haumann et al., 2016].

A

APPENDIX

A.1 STATISTICS OF SOUTHERN OCEAN CARBON SINK

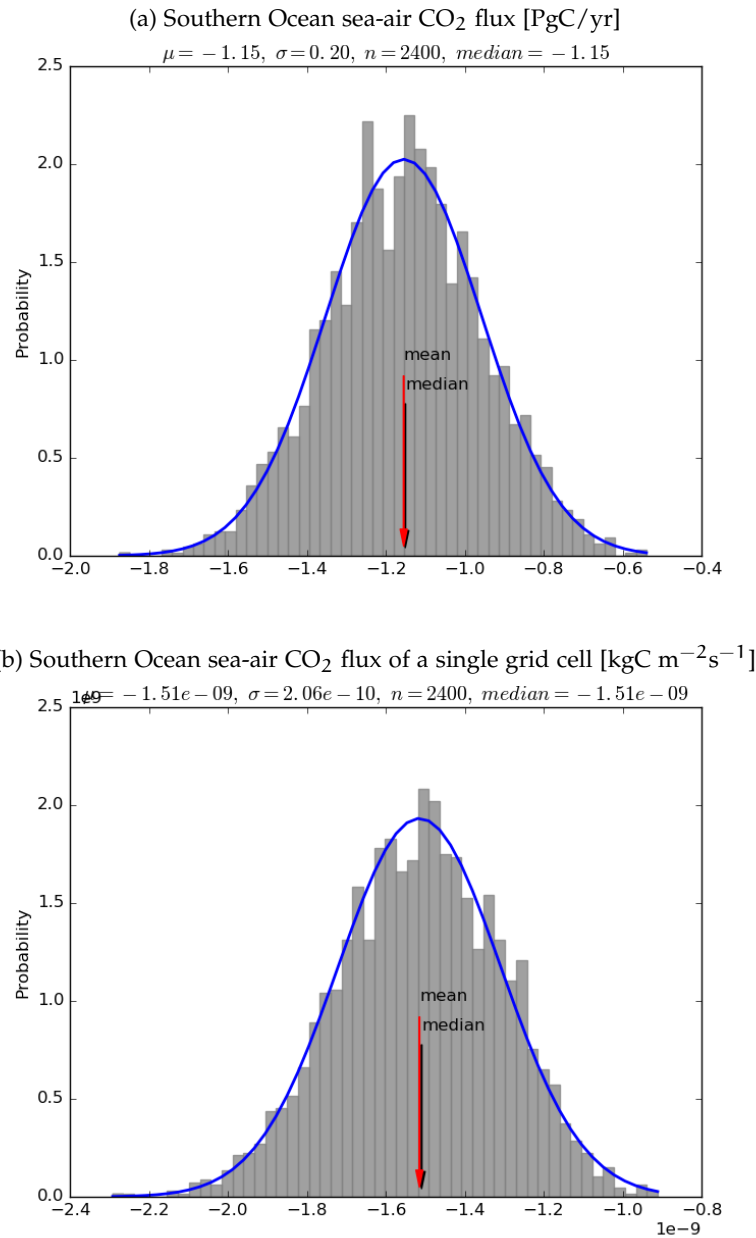


Figure A1: Propability distribution function of the annual sea-air CO₂ flux in the Southern Ocean in ensemble space and temporal space between 1980-2004: (a) field sum over 35-90°S and (b) in a random grid cell.

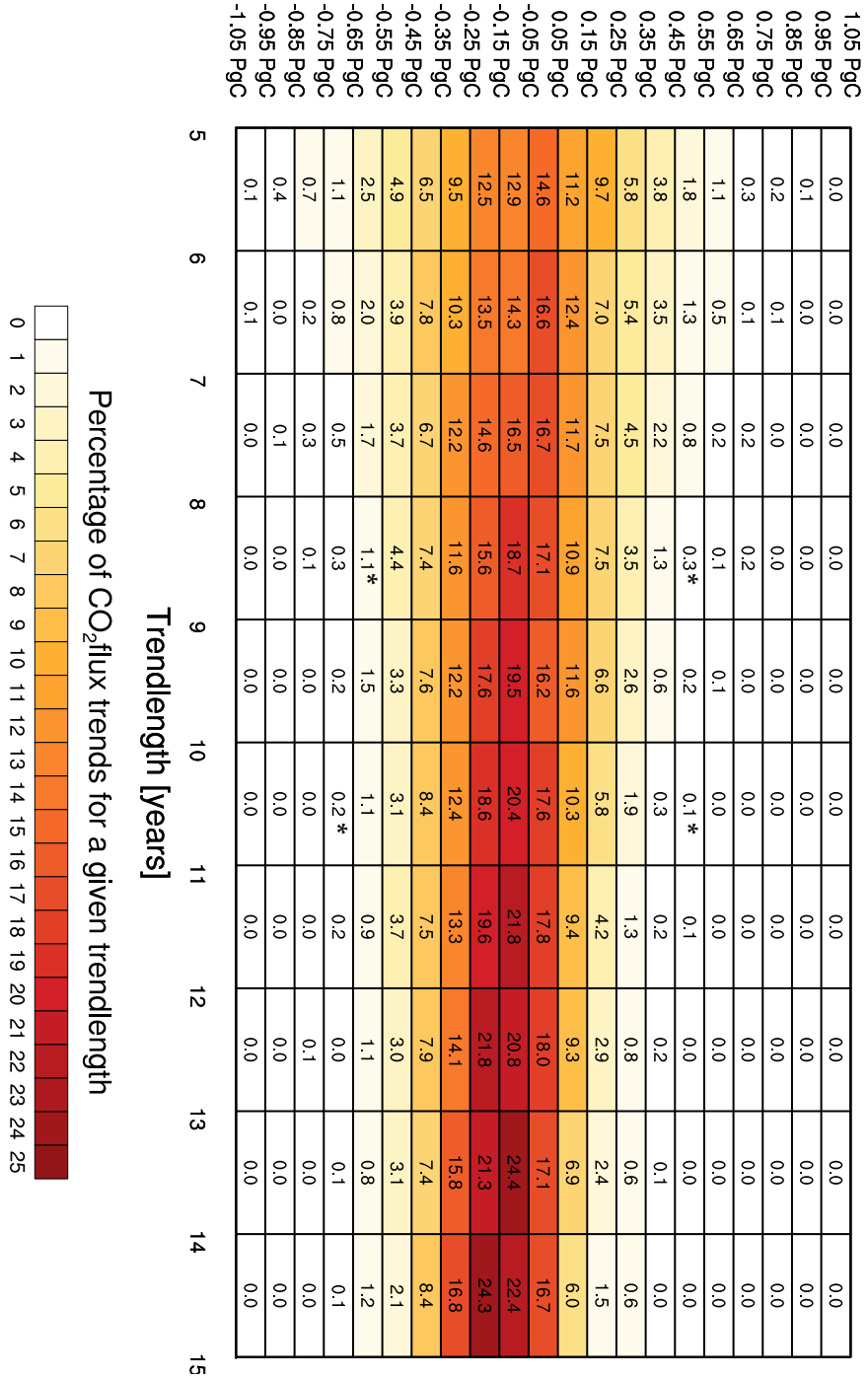
A.2 CO₂ FLUX TRENDSCO₂flux trends heatmap in MPI-ESM Large Ensemble

Figure A2: Southern Ocean carbon sink trends per trend length; * indicate the strongest 8-year and 10-year trends in SOM-FFN

CO₂flux trends heatmap in MPI-ESM Large Ensemble

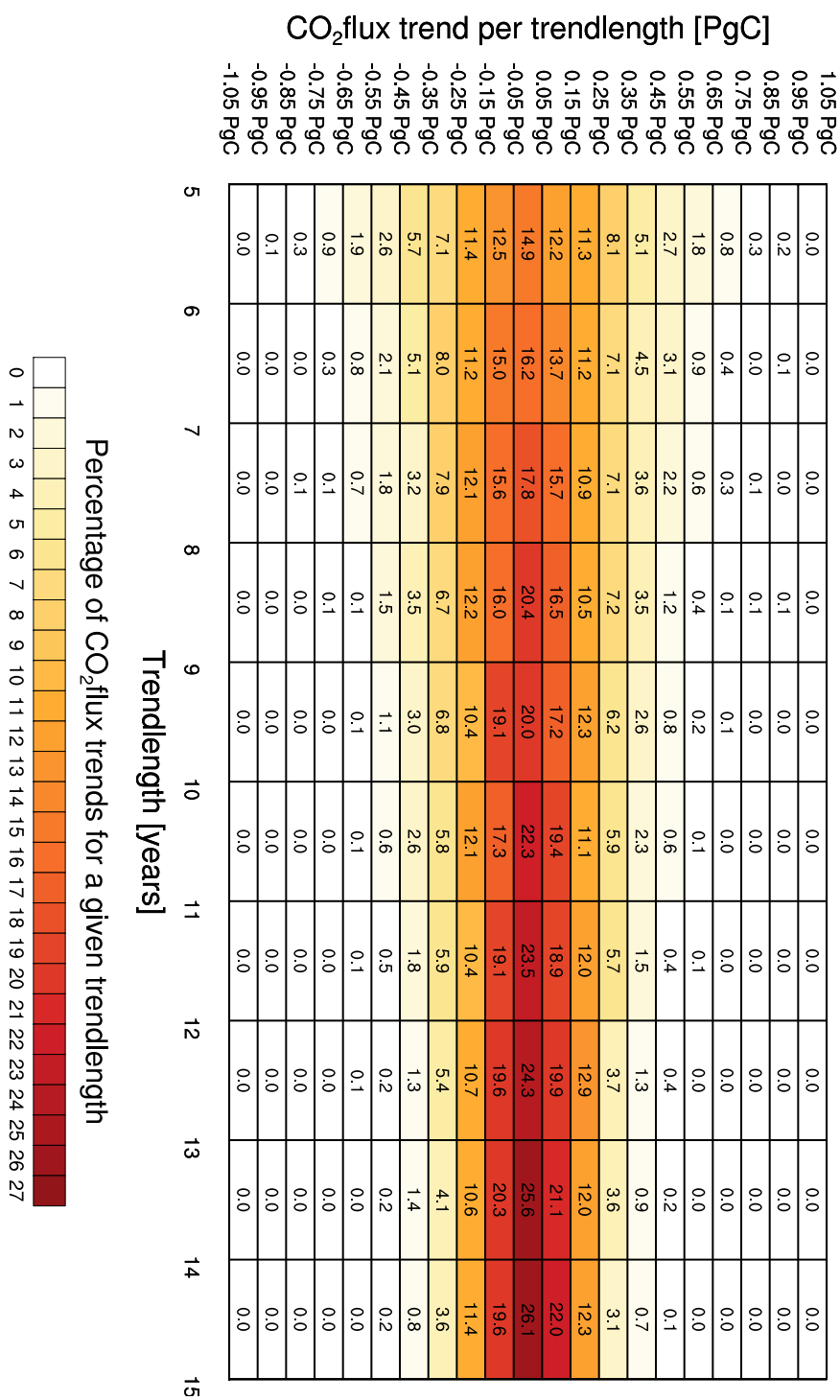


Figure A3: Southern Ocean carbon sink trends per trend length; corrected for forced trend

A.3 MODEL EVALUATION ADDITUM

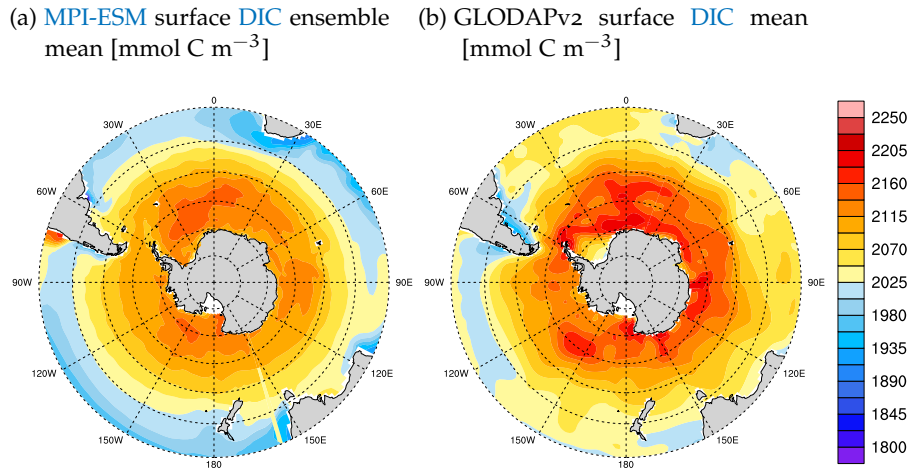


Figure A4: Spatial distribution of the climatology of surface Dissolved Inorganic Carbon (DIC): (a) MPI-ESM LE climatology, (b) GLODAPv2 climatology [Key et al., 2015].

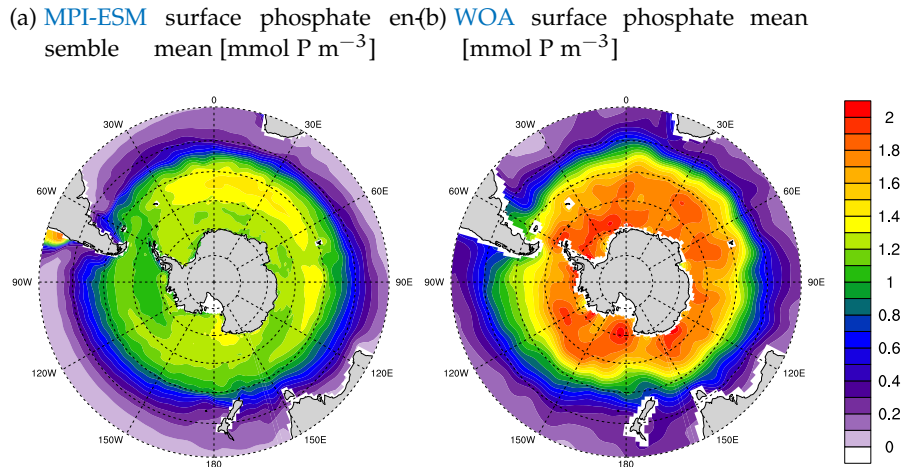


Figure A5: Spatial distribution of the climatology of surface phosphate: (a) MPI-ESM LE climatology, (b) World Ocean Atlas (WOA) climatology [Garcia et al., 2013].

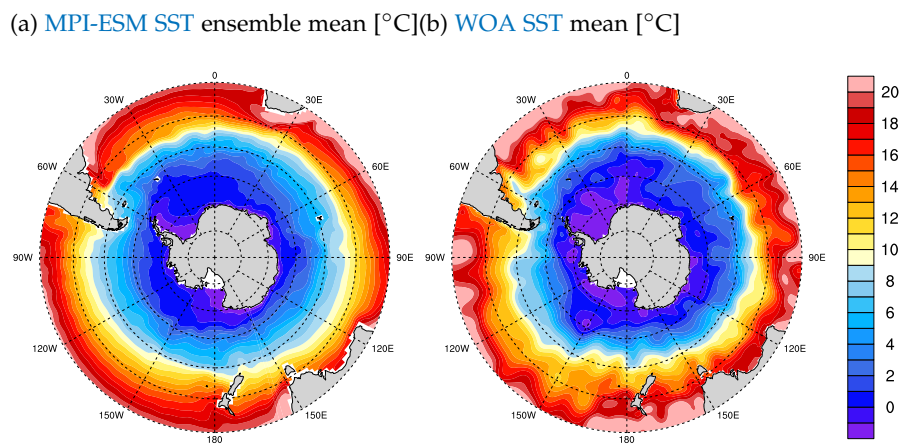


Figure A6: Spatial distribution of the climatology of Sea-Surface Temperature (SST): (a) MPI-ESM LE climatology, (b) WOCE climatology.

A.4 THERMAL SEPARATION BY SEASONS

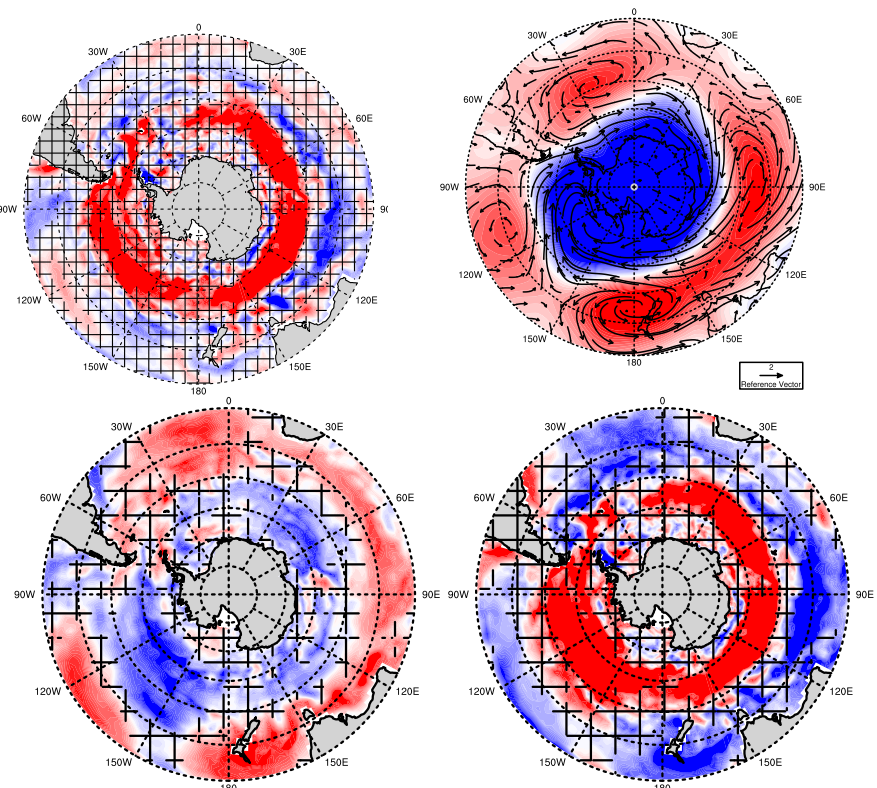
A.4.1 Positive CO_2 flux trend

Figure A7: Linear summer trends for the case of the most positive monotonic 8-year CO_2 flux trend; ΔpCO_2 (a) and sea-level pressure & winds (b); $\text{pCO}_{2,\text{thermal}}$ (c) and $\Delta\text{pCO}_{2,\text{non-thermal}}$ (d); hatched areas indicate where trends are outside the 5% significance level

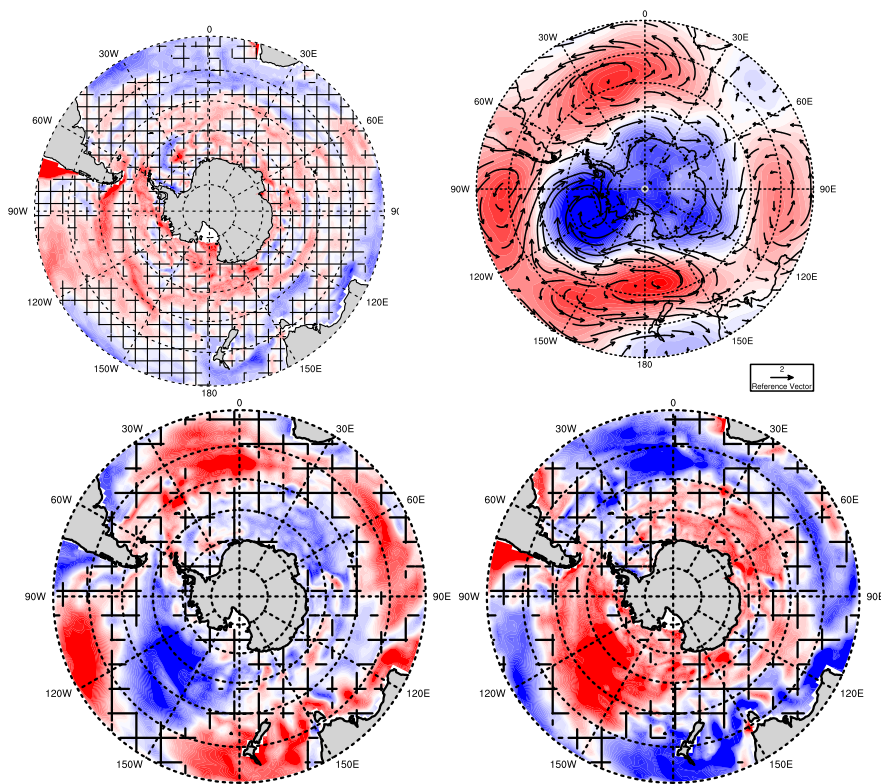


Figure A8: Linear winter trends for the case of the most positive monotonic 8-year CO₂ flux trend; $\Delta p\text{CO}_2$ (a) and sea-level pressure & wind vectors overlaid as arrows (b); $p\text{CO}_2,\text{thermal}$ (c) and $\Delta p\text{CO}_2,\text{non-thermal}$ (d); hatched areas indicate where trends are outside the 5% significance level

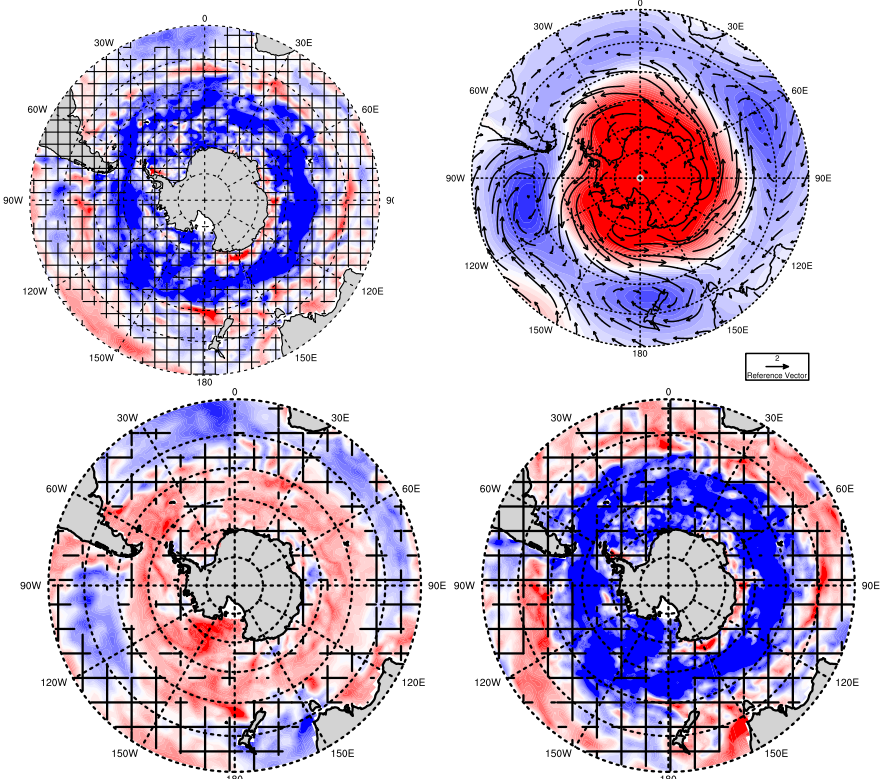
A.5 NEGATIVE CO₂ FLUX TREND

Figure A9: Linear summer trends for the case of the most negative monotonic 8-year CO₂ flux trend; $\Delta p\text{CO}_2$ (a) and sea-level pressure & wind vectors overlaid as arrows (b); $p\text{CO}_{2,\text{thermal}}$ (c) and $\Delta p\text{CO}_{2,\text{non-thermal}}$ (d); hatched areas indicate where trends are outside the 5% significance level

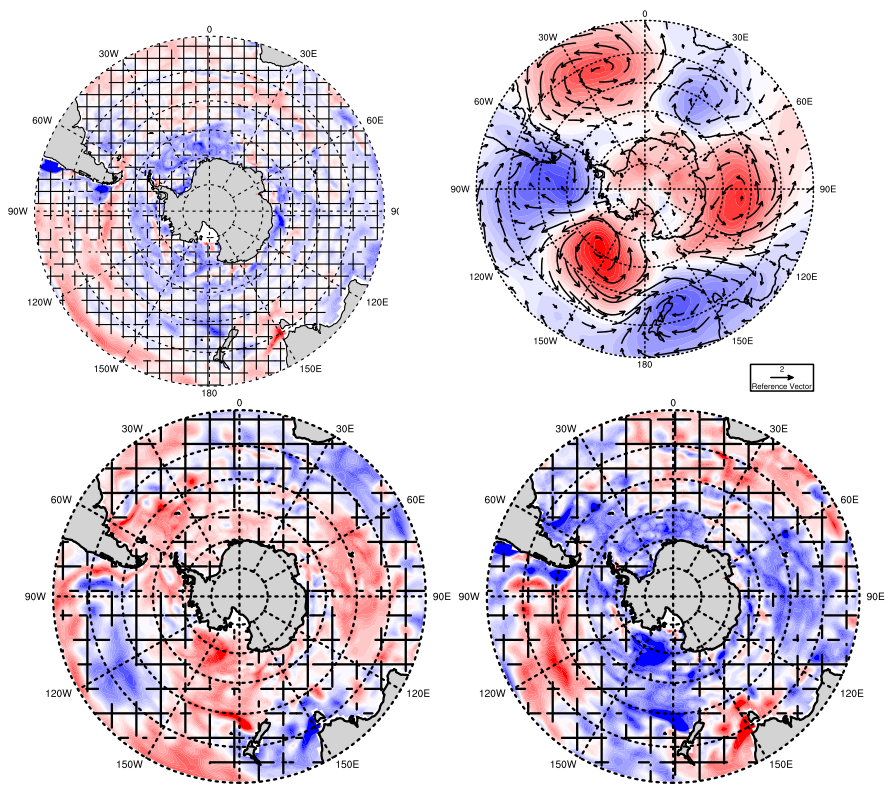


Figure A10: Linear winter trends for the case of the most negative monotonic 8-year CO₂ flux trend; $\Delta p\text{CO}_2$ (a) and sea-level pressure & wind vectors overlaid as arrows (b); $p\text{CO}_{2,\text{thermal}}$ (c) and $\Delta p\text{CO}_{2,\text{non-thermal}}$ (d); hatched areas indicate where trends are outside the 5% significance level

A.6 MIS C

Average phytoplankton growth rate factor [1]

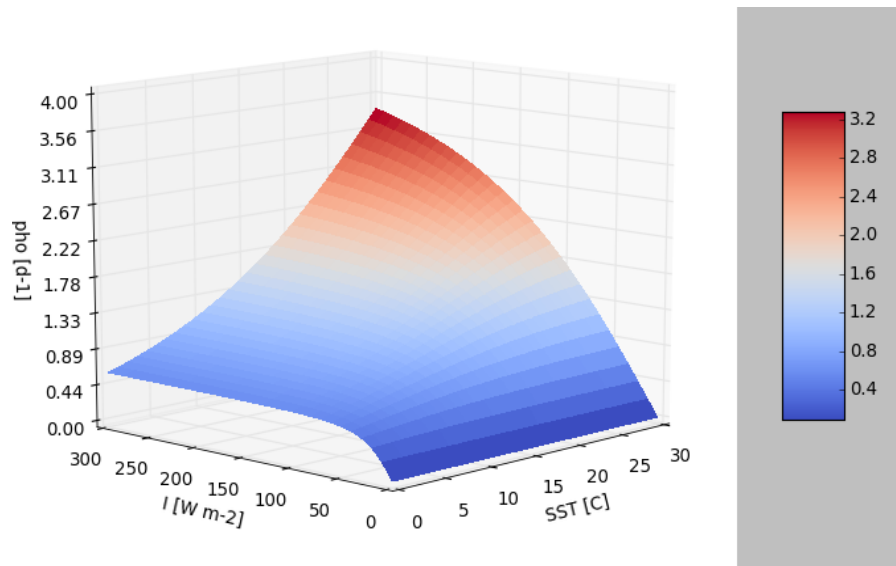


Figure A11: Combined light- & temperature limitation function for the average phytoplankton growth rate in HAMOCC

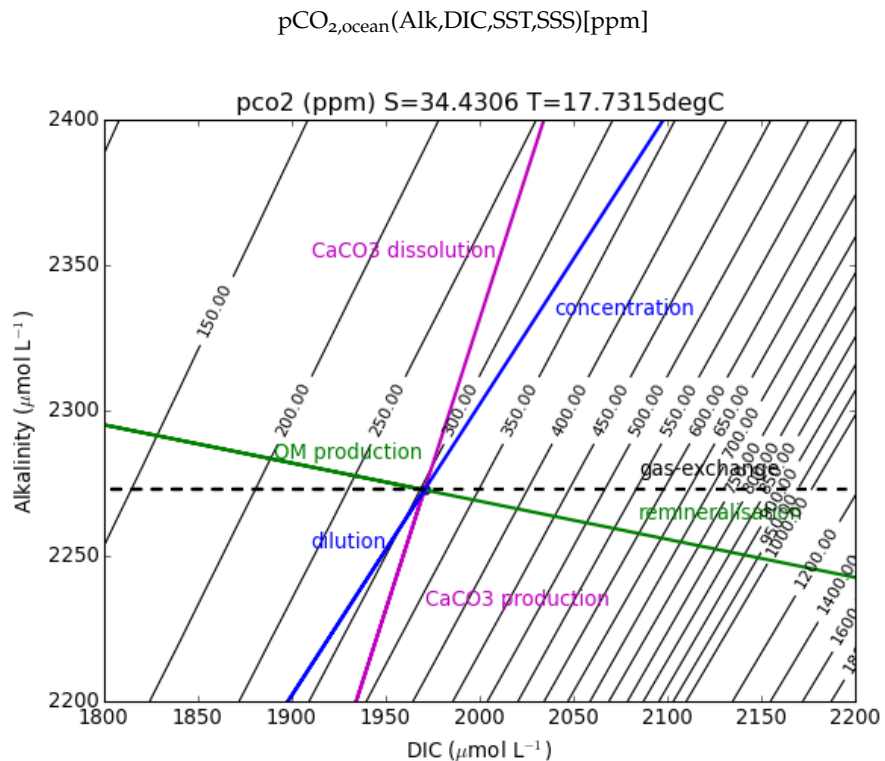


Figure A12: Deffeyes diagram and process contributions

LIST OF FIGURES

Figure 2.1	Schematic overview on the different components in MPI-ESM with prescribed atmospheric partial pressure $p\text{CO}_{2,\text{atm}}$ [Giorgetta et al., 2013]	3
Figure 2.2	Schematic overview of the global ocean biogeochemistry model HAMOCC [Ilyina et al., 2013] which is coupled to the atmospheric model component ECHAM and the ocean model MPIOM . The ocean model provides state variables of physical oceanography, i.e. ice cover, temperature (T), salinity (S) and the advective velocities (\bar{v}). The water column holds tracers of gases, i.e. oxygen (O_2), nitrogen (N_2), laughing gas (N_2O), and dimethyl sulfide (DMS); nutrients, i.e. iron (Fe), phosphate (PO_4), nitrate (NO_3) and silicic acid $\text{Si}(\text{OH})_4$; and tracers of carbonate chemistry, i.e. Dissolved Inorganic Carbon (DIC) and total alkalinity (Alk). Photosynthesis converts DIC and nutrients to Dissolved Organic Carbon (DOC), which produces calcium carbonate (CaCO_3) or opal shells.	5
Figure 3.1	Spatial distribution of the climatology (a,c) and decadal internal variability σ_{DIV} (b,d) from 1980-2004 of the Southern Ocean sea-air CO_2 flux: (a) MPI-ESM LE ensemble mean as forced signal, (b) ensemble decadal standard deviation as decadal internal variability σ_{DIV} , (c) SOM-FFN climatology 1982-2004, (d) SOM-FFN decadal variability σ_{DIV} ; negative values indicate ocean uptake.	14
Figure 3.2	Temporal evolution of the Southern Ocean sea-air CO_2 flux anomaly south of 35°S with respect to the 1980s. Grey lines show the 100 ensemble members, the black line the ensemble mean, the blue shading is the ensemble decadal internal variability σ_{DIV} , the red line shows a positive CO_2 flux trend, the blue line shows a negative CO_2 flux trend, the green line represents the SOM-FFN observation-based estimate [Landschützer et al., 2015]; negative values indicate carbon uptake.	15

Figure 3.3	Spatial distribution of the Southern Ocean Sea-Level Pressure (SLP) and wind vectors overlain as arrows: (a) ensemble mean climatology from 1980 to 2004 as forced signal, (b) ensemble decadal standard deviation as decadal internal variability σ_{DIV} ; (c) difference between MPI-ESM and reanalysis data from NCEP reanalysis climatology [Kalnay et al., 1996], (d) decadal internal variability σ_{DIV} from NCEP reanalysis climatology.	18
Figure 3.4	Temporal evolution of the annual Southern Annular Mode (SAM) index according to [Gong and Wang, 1999]. Grey lines show the 100 ensemble members; the black line the ensemble mean; the blue shading is the decadal internal variability σ_{DIV} ; the red line represents positive CO ₂ flux trend; the blue line shows the negative CO ₂ flux trend; the green line shows the station-based SAM from Marshall, 2003	19
Figure 3.5	Spatial distribution of the vertically integrated primary production in the Southern Ocean: (a) climatological MPI-ESM ensemble mean from 1980 to 2004 as forced signal and (b) ensemble decadal anomaly standard deviation as decadal internal variability σ_{DIV}	21
Figure 3.6	Spatial distribution of surface nitrate in the Southern Ocean: (a) MPI-ESM ensemble mean climatology, (b) World Ocean Atlas (WOA) climatology data [Garcia et al., 2013].	21
Figure 3.7	Temporal evolution of the Integrated Primary Production (INTPP) in the Southern Ocean south of 35°S. Grey lines show the 100 ensemble members, the black line the ensemble mean, the blue shading is the decadal internal variability σ_{DIV} , the red line represents the positive CO ₂ flux trend, the blue line represents negative CO ₂ flux trend.	22

Figure 3.8	Zonally averaged transect of the Southern Ocean and the upper-ocean overturning circulation; black arrows show yearly mean advective transports of (a) water in Sv and (b) carbon in PgC/yr and the related decadal internal variability σ_{DIV} ; white lines are isopyncals separating SAMW at potential density $\rho_\theta = 1026.5 \text{ kg m}^{-3}$ from AAIW , at $\rho_\theta = 1027.2 \text{ kg m}^{-3}$ from CDW , at $\rho_\theta = 1027.7 \text{ kg m}^{-3}$ from AABW ; the black line is the MLD ; the colored contours show the distribution of concentration in DIC	25
Figure 3.9	Spatial distribution of Mixed-Layer Depth (MLD) in the Southern Ocean: (a) MPI-ESM ensemble mean climatology, (b) NOAA Atlas climatology Monterey and Levitus, 1997.	26
Figure 4.1	Linear trends in the SAM as indicator of wind strength vs. CO_2 flux at 50-60°S; each data point represents 8-year trends of a single realization normalized for the ensemble mean trend between 1980 and 2004; the blue dot is the most negative monotonic CO_2 flux trend; the red dot is positive monotonic CO_2 flux trend.	28
Figure 4.2	Linear trends in (a) sea-air CO_2 flux, (b) $\Delta p\text{CO}_2$, (c) SLP and wind vectors overlain as arrows and (d) Sea-Surface Temperature (SST) for the case of the most positive monotonic 8-year CO_2 flux trend; hatched areas indicate where trends are outside the 5% significance level.	30
Figure 4.3	Linear trends in $p\text{CO}_{2,\text{thermal}}$ (a) and $\Delta p\text{CO}_{2,\text{non-thermal}}$ (b) for the case of the most positive monotonic 8-year CO_2 flux trend; hatched areas indicate where trends are outside the 5% significance level.	31
Figure 4.4	Linear trends in (a) Ekman transport and (b) Ekman pumping in the case of the most positive 8-years CO_2 flux trend; hatched areas indicate where trends are outside the 5% significance level.	32

Figure 4.5	Zonally averaged upper-ocean overturning circulation in the case of the most positive 8-year CO ₂ flux trend; black arrows show mean advective carbon transport, red arrows show advective carbon transport trends enforcing the upper-ocean overturning circulation; blue arrows show advective carbon transport trends weakening the upper-ocean overturning circulation; black numbers quantify the trends in advective carbon transport in PgC/8yrs; white lines are isopyncals as in fig. 3.8; grey line is MLD in the beginning and the black line MLD in the end of the period.	33
Figure 4.6	Southern Ocean austral summer trends for the most positive 8-year CO ₂ flux trend: (a) Integrated Primary Production (INTPP), (b) nutrient availability factor, (c) surface temperature & limitation function, (d) Mixed-Layer Depth (MLD), (e) average depth of vertical diffusivity due to wind and (f) phytoplankton average depth; hatched areas indicate where trends are outside the 5% significance level.	36
Figure 4.7	Linear trends in (a) sea-air CO ₂ flux, (b) ΔpCO ₂ , (c) SLP and wind vectors overlain as arrows and (d) Sea-Surface Temperature (SST) for the case of the most negative monotonic 8-year CO ₂ flux trend; hatched areas indicate where trends are outside the 5% significance level.	37
Figure 4.8	Linear trends in pCO _{2,thermal} (a) and ΔpCO _{2,non-thermal} (b) for the case of the most negative monotonic 8-year CO ₂ flux trend; hatched areas indicate where trends are outside the 5% significance level.	38
Figure 4.9	Linear trends in (a) Ekman transport and (b) Ekman pumping in the case of the most negative 8-years CO ₂ flux trend; hatched areas indicate where trends are outside the 5% significance level.	39

Figure 4.10	Zonally averaged upper-ocean overturning circulation in the case of the most negative 8-year CO ₂ flux trend; black arrows show mean advective carbon transport, red arrows show advective carbon transport trends enforcing the upper-ocean overturning circulation; blue arrows show advective carbon transport trends weakening the upper-ocean overturning circulation; black numbers show the trends in advective carbon transport in PgC/8yrs; white lines are isopyncals as in fig. 3.8; grey line is MLD in the beginning and the black line MLD in the end of the period.	40
Figure 4.11	Southern Ocean austral summer trends for the most negative 8-year CO ₂ flux trend: (a) vertically integrated primary production (INTPP), (b) nutrient availability factor, (c) surface temperature & limitation function, (d) Mixed-Layer Depth (MLD), (e) average depth of vertical diffusivity due to wind and (f) phytoplankton average depth; hatched areas indicate where trends are outside the 5% significance level.	42
Figure 5.1	Schematic illustration of pCO ₂ driver separation assuming a well-mixed zonal carbon box of the upper-ocean, where changes in pCO _{2,ocean} are separated into contributions due to sea-air CO ₂ flux (red), thermal effect (orange), the saline effect (yellow), freshwater (light blue), biology (green) and a residual (dark blue) . . .	43

Figure 5.2	Schematic illustration of the Southern Ocean under the context of increasing westerly winds and response in the thermal effect, biology and upper-ocean circulation leading towards a positive CO ₂ flux trend; red color-coding indicates a relative increase of the related quantity or process, whereas blue indicates a relative decrease. Stronger winds enhance the upper-ocean overturning circulation. Increased upwelling increases outgassing of over-saturated deep waters. Increased Ekman transport advects DIC further north, cools the higher latitudes and warms the lower latitudes. Deeper mixing and cooling in the higher latitudes decreases primary production, whereas shallower mixing and warming increase primary production in the lower latitudes. Combined with increasing atmospheric pCO ₂ , the higher latitude outgas strongly, whereas the lower-latitudes slightly ingas.	50
Figure 5.3	Schematic illustration of the Southern Ocean under the context of decreasing westerly winds and response in the thermal effect, biology and upper-ocean circulation leading towards a negative CO ₂ flux trend; red color-coding indicates a relative increase of the related quantity or process, whereas blue indicates a relative decrease. Weaker and northward-shifted winds decrease the upper-ocean overturning circulation, increase primary production at higher latitudes because of deeper mixing and warming. Decreased Ekman transport warms the higher latitudes and reduces Ekman advection, but northward-shifted upwelling increases. Combined with rising atmospheric pCO ₂ , the higher latitudes strongly ingas, whereas the lower-latitudes slight ingas.	53
Figure A1	Probability distribution function of the annual sea-air CO ₂ flux in the Southern Ocean in ensemble space and temporal space between 1980-2004: (a) field sum over 35-90°S and (b) in a random grid cell.	59
Figure A2	Southern Ocean carbon sink trends per trend length; * indicate the strongest 8-year and 10-year trends in SOM-FFN	60

Figure A3	Southern Ocean carbon sink trends per trend length; corrected for forced trend	61
Figure A4	Spatial distribution of the climatology of surface Dissolved Inorganic Carbon (DIC): (a) MPI-ESM LE climatology, (b) GLODAPv2 climatology [Key et al., 2015].	62
Figure A5	Spatial distribution of the climatology of surface phosphate: (a) MPI-ESM LE climatology, (b) World Ocean Atlas (WOA) climatology [Garcia et al., 2013].	62
Figure A6	Spatial distribution of the climatology of Sea-Surface Temperature (SST): (a) MPI-ESM LE climatology, (b) WOCE climatology.	63
Figure A7	Linear summer trends for the case of the most positive monotonic 8-year CO ₂ flux trend; ΔpCO ₂ (a) and sea-level pressure & winds (b); pCO _{2,thermal} (c) and ΔpCO _{2,non-thermal} (d); hatched areas indicate where trends are outside the 5% significance level	64
Figure A8	Linear winter trends for the case of the most positive monotonic 8-year CO ₂ flux trend; ΔpCO ₂ (a) and sea-level pressure & wind vectors overlain as arrows (b); pCO _{2,thermal} (c) and ΔpCO _{2,non-thermal} (d); hatched areas indicate where trends are outside the 5% significance level	65
Figure A9	Linear summer trends for the case of the most negative monotonic 8-year CO ₂ flux trend; ΔpCO ₂ (a) and sea-level pressure & wind vectors overlain as arrows (b); pCO _{2,thermal} (c) and ΔpCO _{2,non-thermal} (d); hatched areas indicate where trends are outside the 5% significance level	66
Figure A10	Linear winter trends for the case of the most negative monotonic 8-year CO ₂ flux trend; ΔpCO ₂ (a) and sea-level pressure & wind vectors overlain as arrows (b); pCO _{2,thermal} (c) and ΔpCO _{2,non-thermal} (d); hatched areas indicate where trends are outside the 5% significance level	67
Figure A11	Combined light- & temperature limitation function for the average phytoplankton growth rate in HAMOCC	68
Figure A12	Deffeyes diagram and process contributions .	68

A.8 LIST OF TABLES

LIST OF TABLES

Table 5.1	Trends in drivers of pCO ₂ for the most extreme positive CO ₂ flux trend and the most most extreme negative CO ₂ flux trend in two 10°-MLD boxes	47
-----------	---	----

ACRONYMS

HAMOCC	HAMBurg Ocean Carbon Cycle Model
ECHAM	European Center for Medium Range Weather Forecasts HAMBurg
MPIOM	Max Planck Institute Ocean Model
ESM	Earth System Model
MPI-ESM	Max Planck Institute-Earth System Model
MPI-ESM LE	Max Planck Institute-Earth System Model Large Ensemble
CMIP5	Coupled Model Intercomparison Project 5
CESM	Community Earth System Model
LE	Large Ensemble
NCAR	National Center for Atmospheric Research
NCEP	National Centers for Environmental Prediction
GFDL	Geophysical Fluid Dynamics Laboratory
NOAA	National Oceanic and Atmospheric Administration
WOA	World Ocean Atlas
SAM	Southern Annular Mode
ENSO	El Niño-Southern Oscillation
DIC	Dissolved Inorganic Carbon
DOC	Dissolved Organic Carbon

INTPP Integrated Primary Production

SST Sea-Surface Temperature

MLD Mixed-Layer Depth

SLP Sea-Level Pressure

ACC Antarctic Circumpolar Current

SAMW Sub-Antarctic Mode Water

AAIW Antarctic Intermediate Water

AABW Antarctic Bottom Water

CDW Circumpolar Deep Water

NPZD NPZD models simulate the interactions of the four variables nutrients (N), phytoplankton (P), zooplankton (Z) and detritus (D).

SOCAT Surface Ocean Atlas

SOM-FFN Self-Organizing Map-Feed-Forward Network

DECLARATION

Erklärung:

Ich versichere, dass ich diese Arbeit selbstständig verfasst habe und keine anderen als die angegebenen Quellen und Hilfsmittel benutzt habe.

Heidelberg, Juni 2017

Aaron Spring